ISPRS Journal of Photogrammetry and Remote Sensing 220 (2025) 354–376

Contents lists available at ScienceDirect

ISPRS Journal of Photogrammetry and Remote Sensing

journal homepage: www.elsevier.com/locate/isprsjprs

# Improving 30-meter global impervious surface area (GISA) mapping: New method and dataset

Huiqun Ren [a], Xin Huang [a,*], Jie Yang [a], Guoqing Zhou [b,c]

[a] School of Remote Sensing and Information Engineering, Wuhan University, Wuhan 430079, PR China
[b] Guangxi Key Laboratory of Spatial Information and Geomatics, Guilin University of Technology, Guilin 541004, PR China
[c] College of Earth Sciences, Guilin University of Technology, Guilin 541004, PR China

ARTICLE INFO

*Keywords:*
Impervious surface area
Long time-series
Omission
Commission
Global

ABSTRACT

Timely and accurate monitoring of impervious surface areas (ISA) is crucial for effective urban planning and sustainable development. Recent advances in remote sensing technologies have enabled global ISA mapping at fine spatial resolution (<30 m) over long time spans (>30 years), offering the opportunity to track global ISA dynamics. However, existing 30 m global long-term ISA datasets suffer from omission and commission issues, affecting their accuracy in practical applications. To address these challenges, we proposed a novel global long-term ISA mapping method and generated a new 30 m global ISA dataset from 1985 to 2021, namely GISA-new. Specifically, to reduce ISA omissions, a multi-temporal Continuous Change Detection and Classification (CCDC) algorithm that accounts for newly added ISA regions (NA-CCDC) was proposed to enhance the diversity and representativeness of the training samples. Meanwhile, a multi-scale iterative (MIA) method was proposed to automatically remove global commissions of various sizes and types. Finally, we collected two independent test datasets with over 100,000 test samples globally for accuracy assessment. Results showed that GISA-new outperformed other existing global ISA datasets, such as GISA, WSF-evo, GAIA, and GAUD, achieving the highest overall accuracy (93.12 %), the lowest omission errors (10.50 %), and the lowest commission errors (3.52 %). Furthermore, the spatial distribution of global ISA omissions and commissions was analyzed, revealing more mapping uncertainties in the Northern Hemisphere. In general, the proposed method in this study effectively addressed global ISA omissions and removed commissions at different scales. The generated high-quality GISA-new can serve as a fundamental parameter for a more comprehensive understanding of global urbanization.

## 1. Introduction

Urbanization is occurring globally, particularly in developing countries such as China and India (Seto et al., 2011; Wang et al., 2012). Extensive urbanization is commonly accompanied by the expansion of impervious surface areas (ISA) (United Nations, 2022). ISA mainly consists of man-made materials such as gravel, asphalt, glass, and metals (Tian et al., 2018), which impede water infiltration and increase runoff volume. Consequently, a series of climate and environmental issues have been triggered, including urban waterlogging, urban heat islands, and water pollution (Fu and Weng, 2016; Li et al., 2019; Zhou et al., 2018). With the 17 Sustainable Development Goals (SDGs) proposed by the United Nations (UN), more attention is being paid to the sustainable development of cities and societies. The global monitoring of ISA can depict the implications of urbanization on the land cover, biodiversity, and environment, which is of great significance for urban planning and sustainable development (Herold et al., 2006; Seto et al., 2012).

Remote sensing technology provides the most practical and cost-effective tool for monitoring global ISA. In recent years, freely accessible satellite data (e.g., Landsat, Sentinel) and powerful cloud platforms (e.g., Google Earth Engine, GEE) have enabled the development of global ISA datasets with high temporal and spatial resolutions (Gómez et al., 2016; Gorelick et al., 2017; Zhu, 2017). For example, the National Geomatics Center of China (NGCC) generated the first operational 30 m global land cover dataset (GlobeLand30) with an ISA layer for the years 2000, 2010, and 2020 (Chen et al., 2015). Subsequently, various organizations and academic institutions successively released 30 m global long time-series (>30 years) ISA datasets, such as global artificial impervious areas (GAIA) (Gong et al., 2020), global annual urban dynamics (GAUD) (Liu et al., 2020), and the global impervious surface area

* Corresponding author at: School of Remote Sensing and Information Engineering, Wuhan University, Wuhan 430079, PR China.
*E-mail address:* xhuang@whu.edu.cn (X. Huang).

https://doi.org/10.1016/j.isprsjprs.2024.12.023
Received 6 July 2024; Received in revised form 12 November 2024; Accepted 24 December 2024
Available online 30 December 2024

(GISA) (Huang et al., 2021), providing a means to monitor ISA changes. Recently, the emergence of 10 m global datasets provide more detailed and accurate ISA information, such as World Settlement Footprint 2019 (WSF2019) (Marconcini et al., 2021), 10 m global impervious surface area (GISA-10) (Huang et al., 2022), and European Space Agency WorldCover (ESA) (Zanaga et al., 2022). However, 10 m global ISA datasets have limited temporal coverage, making it difficult to reflect ISA dynamics over long temporal series. Thus, the 30 m long-term ISA datasets currently remain the preferred choice for tracking global ISA dynamics.

Existing studies suggested that 30 m global long-term ISA mapping suffered from classification uncertainties (Huang et al., 2022; Zhang et al., 2020), including 1) omission errors, i.e., failure to detect ISAs, especially in low-density impervious surfaces (rural, suburban areas); and 2) commission errors, i.e., non-ISAs, such as bare soil and water bodies, being misclassified as ISAs (Wang and Li, 2019; Weng, 2012). As shown in Fig. 1, the 10 m global ISA products consistently show higher impervious areas than the 30 m global ISA products. This phenomenon is caused by uncertainties in these 30 m products, where omission errors may be more significant than commission errors (Zhang et al., 2020). These errors degrade the quality of the datasets and reduce their accuracy in practical applications. Therefore, it is important to address the uncertainties in the current 30 m global long time-series ISA mapping, in order to provide more reliable data for monitoring the urbanization footprint.

For global ISA mapping, supervised classification is the most widely used method. Therefore, training samples, features, and algorithms may lead to the uncertainties (Foody and Arora, 1997; Zhu et al., 2016). Fig. 2 shows four representative examples of omissions and commissions in the current 30 m global long-term ISA datasets, including GISA, GAIA, and GAUD. In rows 1 and 2, GISA, GAIA, and GAUD suffer from omission errors in suburban and rural regions, possibly due to the lack of training samples in these regions. Due to the diversity of ISA types, commonly used sample collection methods, such as manual interpretation and automatic extraction from the existing datasets (Huang et al., 2022; Li et al., 2021), are difficult to cover all kinds of ISA. In rows 3 and 4, GAIA, GAUD, and GISA exhibit commissions caused by high-reflectance bare soil and low-reflectance water bodies. This is likely because these datasets mainly adopted optical features for ISA mapping, which is difficult to separate ISA from other land covers with similar spectra. In summary, omission and commission errors are prevalent in existing 30 m global long time-series ISA datasets, leading to inaccurate statistics and analysis for the global ISA. Against this background, it is essential to develop efficient methods to address these issues.

To address the issue of ISA omissions, a feasible way is to develop an effective ISA monitoring method. Recently, time-series-based change detection algorithms, such as Breaks for Additive Season and Trend (BFAST) (Verbesselt et al., 2010) and Continuous Change Detection and Classification (CCDC) (Zhu and Woodcock, 2014b), have been used to improve the accuracy of long time-series land cover classification. In particular, CCDC has been widely adopted due to its ability to detect multiple land cover changes and its robustness against noise (Chai and Li, 2023; Pasquarella et al., 2022). In most studies, CCDC uses training samples from one point in time to generate time-series land cover maps (Deng and Zhu, 2020), and it classifies the temporal segments (i.e., a period of time) rather than points in time. To obtain satisfactory classification results, the training samples are usually collected from the near-central year of the mapping period (Li et al., 2022). However, training samples from a single year may not comprehensively provide information for different periods. For example, Li et al. (2021) suggested using training samples from multiple years instead of a single year to reduce errors caused by CCDC in time-series land cover mapping.

In addition, detecting newly added ISA is crucial for accurate ISA monitoring. However, the current global ISA samples are often collected from the stable or unchanged areas (Gong et al., 2019b; Huang et al., 2021; Yang and Huang, 2021), and the samples from the ISA change areas are lacking. This exacerbates the difficulties of mapping in these areas. Zhang et al. (2023) pointed out that training a classifier with samples from unchanged areas may not adequately capture the characteristics of change areas. An example is that recently constructed urban areas contain bright roofs with high reflectance, which may not have existed in earlier years. Currently, few studies have focused on collecting ISA samples from change areas. Therefore, there is an urgent need to collect ISA information from change areas to enhance ISA monitoring effectiveness.

On the other hand, with respect to the issue of ISA commissions, methods based on nighttime light data (NTL) have been widely used. These methods used NTL information to distinguish ISA from spectrally similar land covers. For example, Huang et al. (2021) used NTL as a mask to suppress commissions caused by bare soil in arid regions. However, using NTL data alone is not sufficiently effective in reducing commission errors. To enhance this, Gong et al. (2020) integrated NTL

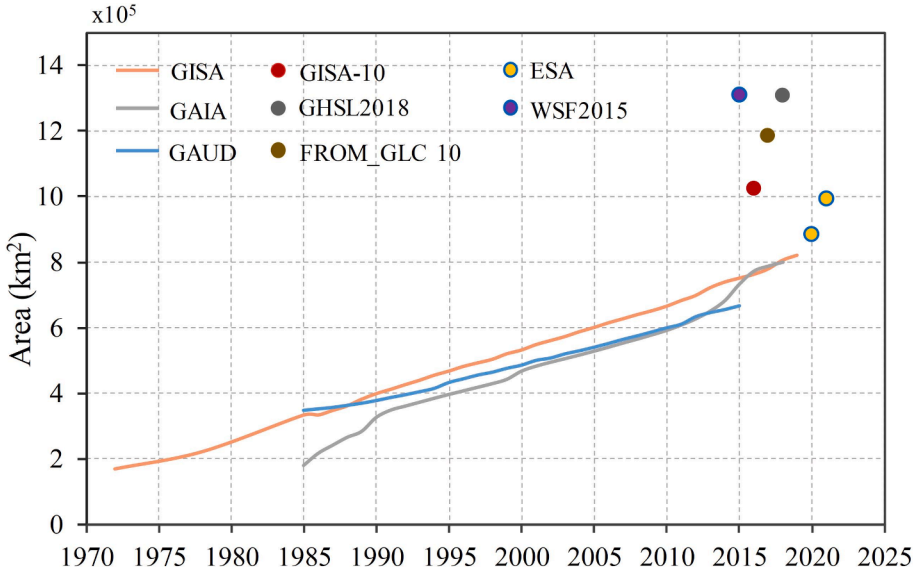


**Fig. 1.** Area statistics of current mainstream high resolution (≤30 m) global ISA products. Time-series curves represent 30 m global long-term ISA products, while scatter points represent 10 m global ISA products.

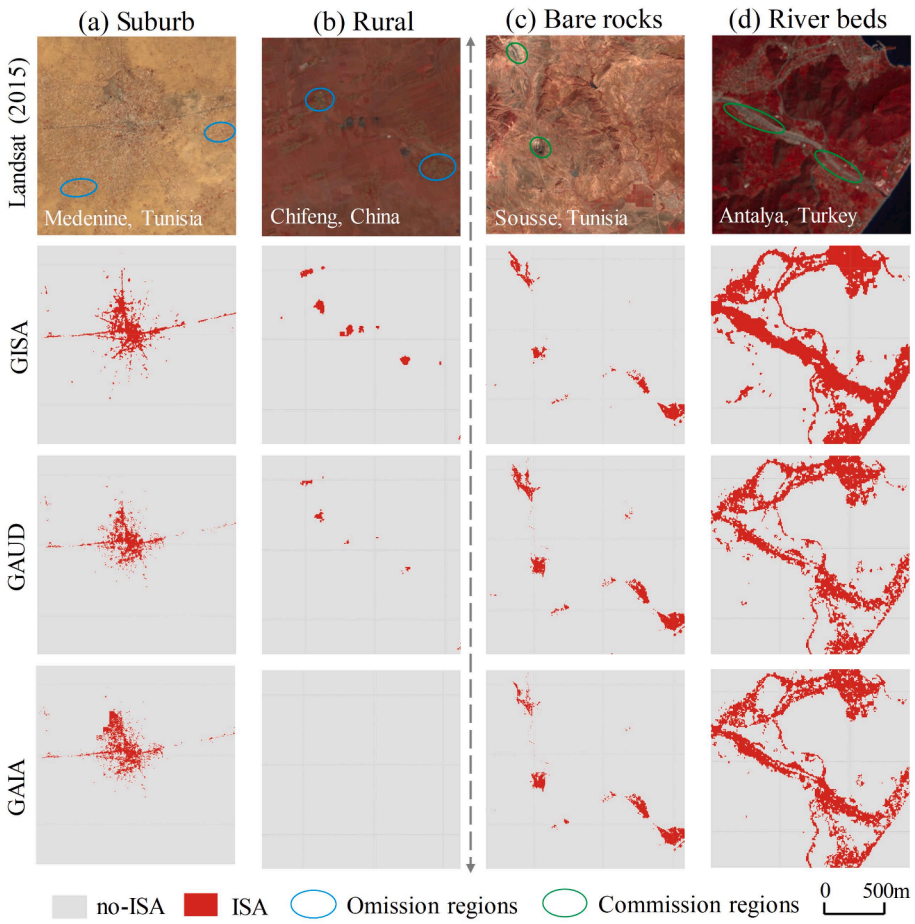


**Fig. 2.** The representative examples of omissions and commissions in the mainstream 30 m global ISA datasets. (a)-(b) represent omission regions: (a) urban-suburban regions in Medenine, Tunisia; (b) small rural settlements in Chifeng, China. (c)-(d) represent commission regions: (c) folded bare land in Sousse, Tunisia; (d) water near the settlements in Antalya, Turkey. Landsat imagery is composited by B5, B4, and B3 in the NIR, red, and green channels for 2015. (For interpretation of the references to color in this figure legend, the reader is referred to the web version of this article.)

and Sentinel-1 SAR data to generate urban masks for arid and semi-arid regions to reduce ISA commissions. Benefiting from the texture information provided by Sentinel-1, this method effectively separated ISA from bare land in arid regions to some extent. However, generating the Sentinel-1 mask required additional training samples collected from urban core areas. Notably, existing high-quality land cover datasets hold great potential for eliminating commission errors with lower labor costs. For example, Esch et al. (2017) used GlobeLand30 directly as reference data to reduce commission errors. However, as shown in Fig. 2 (c)-(d), global ISA commissions exhibit diverse characteristics in terms of their categories and sizes. Currently, however, few studies have considered this issue. Therefore, an effective method for global-scale ISA commission removal remains to be explored.

In summary, to address omission and commission issues in the 30 m global long-term ISA mapping, we proposed a series of new methods and generated a new ISA dataset. The main contributions of this study are as follows:

1) Proposed a multiple temporal CCDC method that accounts for newly added ISA regions (NA-CCDC) to mitigate ISA omissions. The method focuses on collecting multi-temporal newly added ISA samples to strengthen the diversity and representativeness of the samples, thereby improving the accuracy of ISA mapping globally.
2) Proposed a multi-scale iterative (MIA) algorithm for global commission removal, aiming to tackle the diverse characteristics of commission errors, e.g., various types and sizes.
3) Developed a new high-quality 30 m global long time-series ISA dataset from 1985 to 2021, called GISA-new.

The proposed methods in this study are capable of addressing the uncertainty issues (i.e., omission and commission errors) in existing 30 m global continuous ISA products. With the generated new global ISA dataset, it becomes more possible to provide valuable dynamic information for sustainable urban development and support precise global urbanization monitoring.

## 2. Datasets

### 2.1. Satellite data

Two types of satellite data were used in this study: Landsat imagery and night-time light (NTL) data. Landsat imagery was the primary data source for the 30 m global long time-series ISA mapping. Considering that NTL data provides rich information related to impervious surfaces (Zhao et al., 2020), it was employed as reference data to address the commission issue in 30 m global long time-series ISA mapping. Their specific information is described below.

All Landsat surface reflectance (SR) data covering the globe from 1985 to 2021 were collected, including satellite observations from Thematic Mapper (TM), Enhanced Thematic Mapper Plus (ETM + ), and Operational Land Imager (OLI). These Landsat SR data were atmospherically corrected using specific sensor algorithms to eliminate the atmospheric effects on the spectral reflectance of the Earth's surface

(Masek et al., 2006; Vermote et al., 2016). Additionally, clouds and cloud shadows were masked using the C Function of Mask (CFMask) algorithm to obtain clear observation data (Zhu and Woodcock, 2014b). In this study, seven spectral bands from Landsat SR images were selected as input data, including the blue, green, red, near-infrared (NIR), shortwave infrared (SWIR), and thermal bands.

Meanwhile, the monthly VIIRS (Visible Infrared Imaging Radiometer Suite) NTL data of the "vcm" (VIIRS Cloud Mask) version for 2021 was collected, due to its high spatial resolution (~500 m), wide radiometric detection range, and enhanced detection of weaker light (Zheng et al., 2021; Zhou et al., 2021). In this study, annual VIIRS NTL data was generated using the averaging composite method (Elvidge et al., 2021; Wu et al., 2022). However, the annual VIIRS NTL data has background noise from low radiance and extremely high radiance outliers from temporal lights (i.e., aurora and gas combustion), which may affect the accuracy of the NTL data in describing urban areas. Following the methods proposed by Shi et al. (2014) and Ma et al. (2014), we employed the minimum and maximum threshold method to remove background noise and outliers, respectively. Specifically, we determined the minimum threshold as the mean radiance of dark samples (e.g., lakes, reservoirs, and other areas without light) to remove background noise. These dark samples were randomly collected based on Google Earth images. If pixels in annual VIIRS NTL data were lower than the minimum threshold, they were identified as background noise and assigned to zero. On the other hand, we set the maximum threshold as the maximum radiance of airport data to remove outliers. The airport's data recorded the location of 75,786 large airports globally (https://ourairports.com, last access: 17 August 2022) and was manually checked to ensure its correctness. If pixels in the VIIRS NTL data were higher than the maximum threshold, they were recognized as outliers and assigned to the maximum threshold.

### 2.2. Global 10 m ISA datasets

Compared to the 30 m global ISA dataset, the 10 m global ISA datasets demonstrate superior performance (Huang et al., 2022), providing high-quality data for addressing uncertainties (e.g., omission and commission errors) in the existing 30 m global long-term ISA datasets. In this study, two 10 m global ISA datasets were selected as (1) reference data and (2) training sample sources. The first dataset is the global land cover developed by the European Space Agency (abbreviated as ESA WorldCover). The built-up layer in the ESA WorldCover for 2020 and 2021 was used, with definitions consistent with GISA-new (Zanaga et al., 2020; Zanaga et al., 2022). The second dataset is World Settlement Footprints 2019 (WSF 2019), outlining the worldwide human settlement extent for the nominal year 2019. The WSF 2019 was generated using a novel method that combines multi-temporal Sentinel-1 and Sentinel-2 imagery, enhancing the detailed description of human settlements and achieving an accuracy range of 83 %-89 % (Cai et al., 2023; Marconcini et al., 2021). To match the spatial resolution of GISA-new, the two 10 m global ISA datasets were resampled to 30 m resolution using a class synthesis strategy (Liu et al., 2020a).

### 2.3. Building data

To achieve more accurate global ISA mapping, two building-related datasets were also used to address ISA omissions. The first one is the building footprint data released by Microsoft (Microsoft, 2022). Microsoft's building footprint includes 770 million building polygons with an accuracy of over 90 %. However, this information is missing for China. Therefore, the second building dataset used in this study is the vectorized rooftop area data for 90 cities in China (Zhang et al., 2022c). The rooftop area data, created by Nanjing Normal University in 2020, contains over 200 million building polygons. Through the validation based on testing data covering 180 $km^2$ across different regions, its overall accuracy and F1-score are 97.95 % and 83.11 %, respectively. Considering the high quality of the two building datasets, it is potential to use them as training sample sources.

### 2.4. Global 30 m long time-series ISA datasets

Four global 30 m long time-series ISA datasets, including GAIA, GAUD, GISA, and WSF-evo (World Settlement Footprint-Evolution), were used to compare with our GISA-new. These datasets are described below. GAIA is an annual global ISA map at 30 m resolution from 1985 to 2018, produced by combining multi-source satellite imagery (e.g., Landsat, NTL, and Sentinel 1) and the 'Exclusion-Inclusion' algorithm (Gong et al., 2020). GAUD is a global urban change dataset for the time period of 1985–2015, generated by applying a time-series segmentation method based on the NUACI index of Landsat imagery (Liu et al., 2020). GISA is the longest time-series global ISA dataset with 30 m resolution, using over three million Landsat images and a novel mapping method that integrates semi-automatic global sample collection, local adaptive classification, and spatiotemporal post-processing (Huang et al., 2021). WSF-evo is a global human settlement extent dataset on a yearly basis from 1985 to 2015, generated using an iterative technique that first extracts training samples for each year in reverse chronological order from an urban mask and then classifies Landsat 5/7 imagery using RF algorithm (Marconcini et al., 2021).

## 3. Methodology

The objective of this study is to reduce the omission and commission errors in existing 30 m global long time-series ISA datasets and generate a new high-precision global ISA dataset (called GISA-new). Given that GISA (our previous version) has the longest time span (from 1985 to 2021) and reliable accuracy, it was selected as a benchmark in this study. As shown in Fig. 3, we first identified the potential omission and commission regions in GISA (Section 3.1). Then, we proposed a multi-temporal CCDC algorithm that accounts for newly added ISA regions (NA-CCDC) to reduce omission errors (Section 3.2). Afterward, we proposed a multi-scale iterative algorithm (MIA) to remove commission errors at a global scale (Section 3.3). Finally, we fused the above results to create a new annual global ISA product from 1985 to 2021 (i.e., GISA-new) and assessed its accuracy using independent test samples (Section 3.4).

### 3.1. Identifying potential omission and commission regions

First, we identified the regions of omission or commission errors in GISA (Fig. 3(a)). The WSF2019 and ESA datasets were used as references, as their mapping years are close to 2021 and they are reported with satisfactory mapping performance (Section 2.2). Additionally, building footprints (in vector format), including Microsoft's building footprint (Microsoft, 2022) and vectorized rooftop area data for 90 cities in China (Zhang et al., 2022) (Section 2.3), were incorporated to further reduce omission errors. Specifically, we first extracted the 2021 map from GISA (denoted as GISA-2021). Next, we computed the union of ESA, WSF2019, and building footprints to create the maximum ISA extent (denoted as $MaxExtent_{ISA}$). In this study, the WSF 2019, ESA, and building footprints were resampled to 30 m. Specifically, if a 30 m × 30 m area contains the ISA pixels at the 10 m resolution with a certain percentage threshold, it is labeled as ISA; otherwise, it is labeled as non-ISA. A larger threshold would generate purer training samples but may result in more omissions and fewer commissions, while a smaller threshold would reduce omission errors but increase commission errors. In this study, in terms of the IGBP (International Geosphere-Biosphere Programme) classification system (Loveland and Belward, 1997), we set the threshold as 30 %. The IGBP system was chosen because it is the most widely used global Land Use/Land Cover (LULC) classification system (Sulla-Menashe et al., 2019; Wang et al., 2023). Finally, we spatially overlaid $MaxExtent_{ISA}$ with GISA-2021 to detect potential

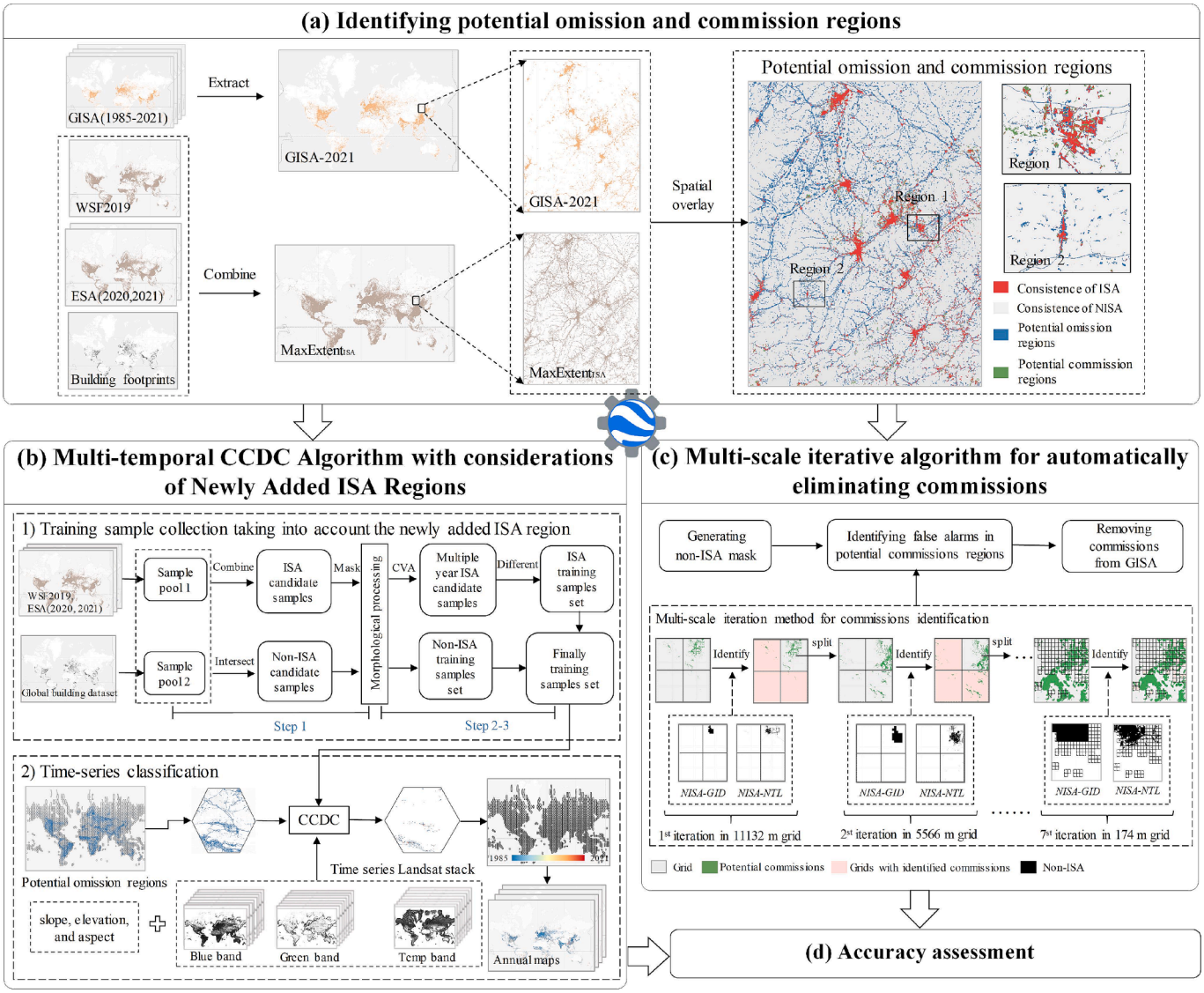


**Fig. 3.** The flowchart for generating GISA-new.

omission and commission regions. The potential omission regions were those pixels classified as ISA in $MaxExtent_{ISA}$ but as non-ISA in GISA-2021. The potential commission regions were those pixels classified as ISA in GISA-2021 but as non-ISA in $MaxExtent_{ISA}$.

It is worth noting that the potential omission or commission regions indicate that GISA may contain omission or commission errors. To further confirm the presence of these errors, we developed specific algorithms for these regions. Specifically, for potential omission areas, a multi-temporal CCDC algorithm that accounts for newly added ISA regions (NA-CCDC) was proposed. This method collected multi-temporal newly added ISA samples to enhance the diversity of sampling and then used the CCDC algorithm to detect ISA in the potential omission regions. As for the potential commission areas, a multi-scale iterative (MIA) algorithm was proposed. Given the diversity of ISA commissions in terms of sizes and types, this method employed an iterative strategy on grids with various scales to automatically identify and remove ISA commissions on a global scale.

### 3.2. NA-CCDC algorithm

To address the global omission issue, we developed an efficient mapping method for the potential omission regions. Considering that the mapping task refers to a large-scale and long time span, a time-series-based change detection method, i.e., the CCDC algorithm, was adopted in this study. The CCDC algorithm commonly uses training samples derived from one temporal point for land cover classification (Wang et al., 2024; Xie et al., 2022). However, the diversity and complexity of ISA types, especially in newly added ISA regions (NIR), increase the requirement for ample time-series training samples. Therefore, we proposed a multiple-temporal CCDC algorithm that accounts for newly added ISA regions (NA-CCDC), consisting of two parts: 1) training samples generation considering NIR; and 2) time-series classification.

#### 3.2.1. Training samples generation considering newly added ISA regions

Most previous studies commonly collected training samples from existing datasets in an automated manner (Huang et al., 2022; Li et al., 2021). However, existing 30 m global long-term ISA datasets suffer from omissions and commissions, which may affect the quality of the training samples (Fig. 2). Therefore, high-quality 10 m global ISA datasets (i.e., ESA and WSF2019) and building data were introduced as training sample sources in this study. However, their mapping years are limited (around the year of 2021). To construct multi-temporal training samples, a transfer strategy was applied to obtain earlier years' samples. Subsequently, NIR samples were created using a differential operation.

Details are presented in the following.

Step 1: Generating candidate samples using a fusion strategy (Fig. 5 (a)). We fused the 10 m global ISA dataset (i.e., ESA and WSF2019) and building data to enhance the diversity of the training samples. Furthermore, considering the uncertainty of training sample sources, a series of screening processes were utilized to ensure the reliability of the samples. Specifically, the consistent areas of ESA and WSF2019 were viewed as sample pool 1 through an intersection operation. Meanwhile, referring to the recommendations of Hafner et al. (2022), the grids (in 30 m by 30 m) whose ratios of buildings were more than 50 % were viewed as ISA, to generate the sample pool 2. Sample pools 1 and 2 were fused to create ISA/non-ISA candidate samples. Specifically, ISA candidate samples were those classified as ISA in either sample pool 1 or sample pool 2 (Zhang et al., 2022a), to improve the diversity of samples. Non-ISA candidate samples were those classified as non-ISA in both sample pools. Finally, morphological processing (i.e., erosion) was conducted on ISA/non-ISA candidate samples to remove mixed pixels along the boundary. It should be noted that referring to the 10 m global ISA dataset and building footprint data, the candidate samples are for the year 2021. As shown in Fig. 4 (c), the ISA information fusion provides more samples for potential omission regions.

Step 2: Transferring ISA candidate samples (Fig. 5(b)). To generate multi-temporal ISA candidate samples, we iteratively transferred the 2021 ISA candidate samples to the previous years. In this study, the previous years were selected at 10-year intervals, including 1990, 2000, and 2010. To achieve the transferring, change vector analysis (CVA) was chosen due to its wide application in a large number of studies in land cover change and urban dynamics (Bovolo and Bruzzone, 2007; Huang et al., 2020; Li et al., 2018). Since the mapping of potential omission regions was stratified by a 2° hexagon (Section 3.2.2), CVA was conducted for each hexagon in each previous year. Specifically, the feature vectors between 2021 and the corresponding previous year (e.g., 2010, 2000, 1990) were input into the CVA to generate the change intensity map. The feature vectors comprise the mean and variance of annual NDVI, MNDWI, and NDBI. Subsequently, the local Otsu method was applied to the change density map to automatically determine the change/no-change threshold. Regions with no change were retained as ISA candidate samples. After CVA, multi-temporal ISA candidate samples were acquired, including the years of 1990, 2000, 2010, and 2021.

Step 3: Generating NIR ISA candidate samples (Fig. 5(c)). Newly added ISA regions (NIR) are defined as pixels classified as non-ISA in the previous-year map but classified as ISA in the later-year map. To this end, we applied a differential operation on multi-temporal ISA candidate samples to derive NIR candidate samples. Taking 2021 as an example, NIR candidate samples refer to pixels classified as non-ISA in the 2010 ISA candidate samples, but classified as ISA in the 2021 ISA candidate samples. Finally, we combined all the NIR samples as the final ISA training samples set.

Based on the above steps, the final ISA training sample set was generated by the multi-temporal sample migration and considering the newly added ISA region samples. Meanwhile, the 2021 non-ISA candidate samples were also included into the final non-ISA training sample set (Fig. 3(b1)). This is because the transition from ISA to non-ISA is typically irreversible, so the 2021 non-ISA candidate samples can be directly applied to other years (Zhang et al., 2022b).

### 3.2.2. *Time-series classification*

In this study, we executed the local CCDC algorithm by dividing the

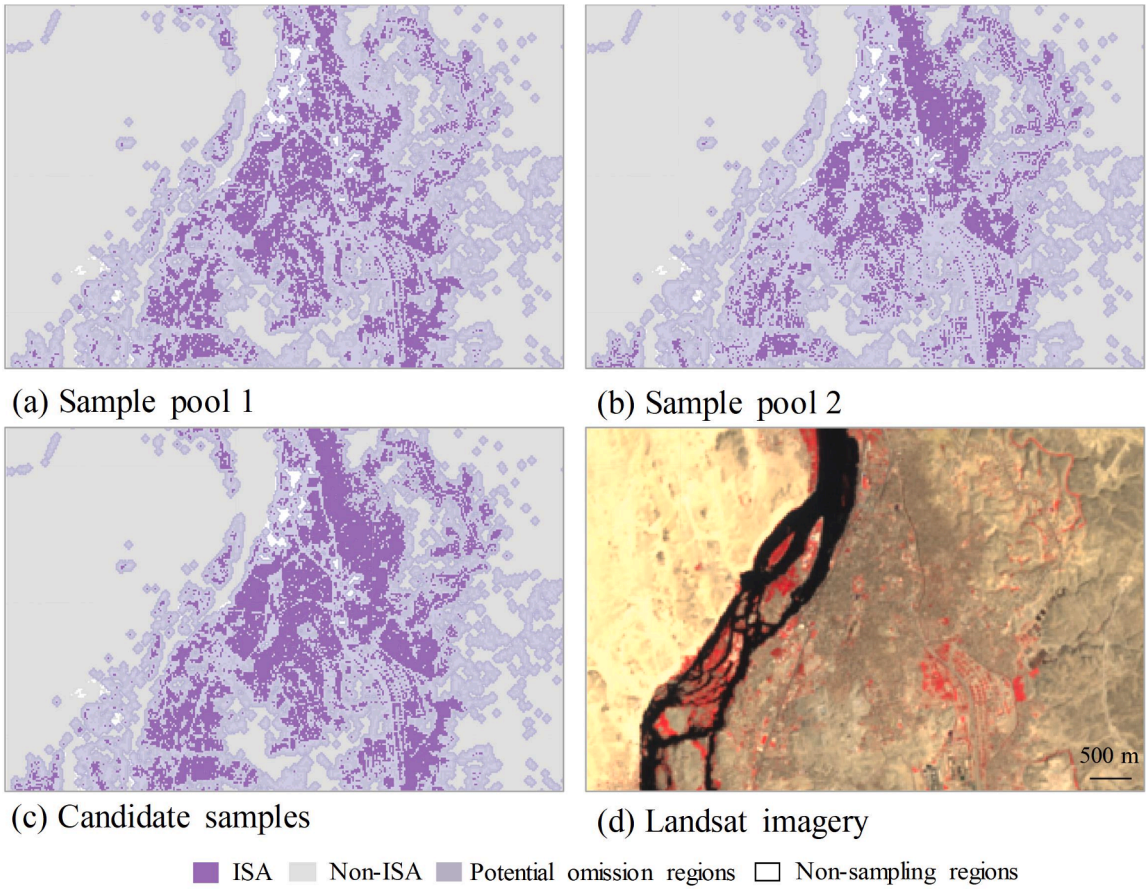


**Fig. 4.** The process of generating candidate samples, with (a) Sample Pool 1 from the existing datasets, (b) Sample Pool 2 from the building footprint data, (c) Candidate samples, and (d) Potential omission regions that need re-classification with additional samples. Landsat imagery, which is composited by NIR, red, and green channels in the year 2020. (For interpretation of the references to color in this figure legend, the reader is referred to the web version of this article.)

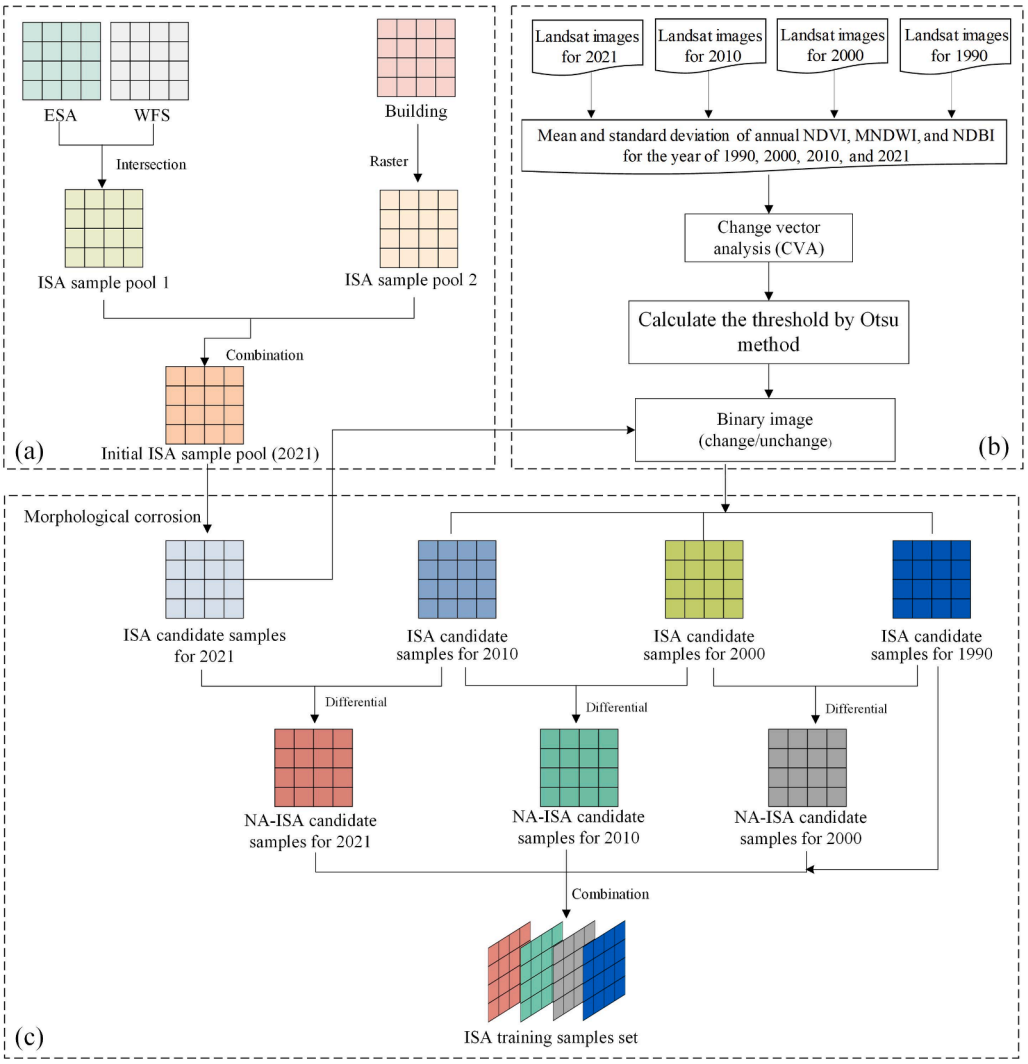


**Fig. 5.** The workflow of the newly added ISA (NA-ISA) sampling strategy. (a) generating initial ISA samples pool using fusion sampling. (b) generating multi-temporal samples using the transfer method. (c) generating NIR samples based on differential operations.

potential omission regions into hexagonal grids with 2° sides. The CCDC algorithm consists of two parts, i.e., Continuous Change Detection (CCD) and Classification (Zhu and Woodcock, 2014b). In the CCD part, all the time-series Landsat observations were used to detect changes at the pixel level by fitting the harmonic regression model. The identified break-points segment the entire time series into several sub-time series, each corresponding to a regression model whose coefficients (equation (1) and (2)) were used for classification.

$$\hat{\rho}(i,x) = a_{0,i} + c_{1,i}x + \sum_{k=1}^{3}\left(a_{k,i}\cos\left(\frac{2k\pi}{T}x\right) + b_{k,i}\sin\left(\frac{2k\pi}{T}x\right)\right) \quad (1)$$

where $\hat{\rho}(i,x)$ represents the predicted value for the Landsat band $i$ at Julian date $x$ ,$a_{0,i}$ represents the overall value (i.e., intercept) for the Landsat band $i$, $c_{1,i}x$ represents the inter-year change coefficients (i.e., slop) for the Landsat band $i$, $a_{k,i}$ and $b_{k,i}$ represent the intra-year change coefficients, T represents the number of days per year.

$$\bar{\rho} = a_{0,i} + c_{1,i} \times \frac{t_{start} + t_{end}}{2} \quad (2)$$

where $\bar{\rho}$ represents the overall value at the center of each regression model for each Landsat band, $t_{start}$, and $t_{end}$ represents the start and end dates of the regression model, respectively.

In the classification part, each sub-time series was classified as a land cover type (ISA or non-ISA) using a random forest (RF) classifier. As advised by Zhang et al. (2020), the key parameters in the RF, namely the number of trees and the number of predictor variables, were set to 500 and the default value (i.e., the square root of the number of features), respectively. The RF was trained in each hexagonal grid using classification features and training samples. Specifically, the classification features consist of the regression model coefficients (e.g., $c_{1,i}$, $a_{k,i}$, $b_{k,i}$, $\bar{\rho}$, and RMSE) and ancillary data (e.g., slope, elevation, and aspect) derived from the Shuttle Radar Topography Mission (SRTM) and ALOS World

**Table 1**
Classification features used for CCDC.

| Name | Features |
|---|---|
| Blue | $\bar{\rho}_{Blue}$,$c_{1,Blue}$ $a_{1,Blue}$, $b_{1,Blue}$, $a_{2,Blue}$, $b_{2,Blue}$, $a_{3,Blue}$, $b_{3,Blue}$, and $RMSE_{Blue}$ |
| Green | $\bar{\rho}_{Green}$,$c_{1,Green}$ $a_{1,Green}$, $b_{1,Green}$, $a_{2,Green}$, $b_{2,Green}$, $a_{3,Green}$, $b_{3,Green}$, and $RMSE_{Green}$ |
| Red | $\bar{\rho}_{Red}$,$c_{1,Red}$ $a_{1,Red}$, $b_{1,Red}$, $a_{2,Red}$, $b_{2,Red}$, $a_{3,Red}$, $b_{3,Red}$, and $RMSE_{Red}$ |
| NIR | $\bar{\rho}_{NIR}$,$c_{1,NIR}$ $a_{1,NIR}$, $b_{1,NIR}$, $a_{2,NIR}$, $b_{2,NIR}$, $a_{3,NIR}$, $b_{3,NIR}$, and $RMSE_{NIR}$ |
| SWIR1 | $\bar{\rho}_{SWIR1}$,$c_{1,SWIR1}$ $a_{1,SWIR1}$, $b_{1,SWIR1}$, $a_{2,SWIR1}$, $b_{2,SWIR1}$, $a_{3,SWIR1}$, $b_{3,SWIR1}$, and $RMSE_{SWIR1}$ |
| SWIR2 | $\bar{\rho}_{SWIR2}$,$c_{1,SWIR2}$ $a_{1,SWIR2}$, $b_{1,SWIR2}$, $a_{2,SWIR2}$, $b_{2,SWIR2}$, $a_{3,SWIR2}$, $b_{3,SWIR2}$, and $RMSE_{SWIR2}$ |
| Temp | $\bar{\rho}_{temp}$,$c_{1,temp}$ $a_{1,temp}$, $b_{1,temp}$, $a_{2,temp}$, $b_{2,temp}$, $a_{3,temp}$, $b_{3,temp}$, and $RMSE_{temp}$ |
| Ancillary data | slope, elevation, and aspect |

3D-30 m (AW3D30) (Table 1). On the other hand, training samples were randomly collected from the final training sample set (Section 3.2.1) using stratified sampling. In detail, for each hexagon, 18,000 samples were extracted, including 15,000 non-ISA and 3,000 ISA. It's worth noting that the sample size for NIR was set at 1,500 (half of the total training samples) to strengthen the representativeness of the samples in the newly added ISA areas. After classification, the annual ISA maps were generated in the potential omission regions from 1985 to 2021.

### 3.3. MIA algorithm for commission removal

In current literature, NTL data is commonly used as a mask for suppressing ISA commissions (Gong et al., 2019a; Huang et al., 2021). Given the coarse resolution of NTL, it is insufficient to remove commissions using this data alone (Gong et al., 2020). Therefore, the 10 m global ISA dataset was introduced in this study to improve the effectiveness of commission removal. It should be noted that global commissions present diversity in terms of their categories and sizes. For example, commissions were caused by different land covers (e.g., bare soil and water bodies) and had different sizes (Fig. 2 (c)-(d)). However, existing studies rarely consider the characteristics of commissions. To address this issue, we proposed a multi-scale iterative algorithm (MIA) for automatically identifying and removing commissions at a global scale, which consists of three main steps: 1) generating non-ISA mask layers; 2) identifying global commission errors; and 3) removing commission errors.

Firstly, two non-ISA mask layers were generated from the 2021 VIIRS NTL data and the 10 m global ISA datasets (i.e., ESA and WSF 2019), respectively. The VIIRS NTL data was utilized due to its advantage in detecting low-level nighttime light, which is more suitable for accurately describing ISA extent (Zheng et al., 2021; Zhou et al., 2021). The ESA and WSF 2019 were selected because of their good performance among the available 10 m global ISA datasets (see Section 2.2). We named the mask layer generated from the VIIRS NTL data as *NISA-NTL* and the mask layer derived from the 10 m global ISA datasets as *NISA-GID*. The *NISA-NTL* was obtained from the VIIRS NTL data using a defined threshold. According to Huang et al. (2021), we set this threshold to 3. The *NISA-NTL* was defined as those pixels with values less than 3 in the VIIRS NTL data. On the other hand, the *NISA-GID* was gained by performing an intersection operation on ESA and WSF 2019 to ensure the quality of the mask layer. The *NISA-GID* was defined as those pixels classified as non-ISA in both ESA and WSF 2019.

We proposed a multi-scale iterative strategy based on the non-ISA mask layer to identify commissions in potential commission regions. Previous studies typically identified commissions based on non-ISA mask information at the pixel level, where ISA pixels corresponding to non-ISA pixels in the mask layer were identified as commissions (Liu et al., 2018). However, pixel-level information is sensitive to noise. Therefore, we utilized non-ISA mask information at the grid level to iteratively identify commissions. If the non-ISA mask layer completely covers a grid cell, the ISA pixels within the grid are considered commissions. To ensure the accuracy of identification, both non-ISA mask layers (i.e., *NISA-GID* and *NISA-NTL*) need to meet this condition. Considering the diversity of global commissions in terms of categories and scales, we first divided the potential commission regions into grid cells of different sizes and then adopted an iterative strategy on these grids to identify commissions (see Algorithm 1). In detail, we initially divided the potential commission regions into a square grid with a length of 0.1° (about 10 km), labeled as $G$. For each grid $G_i$, we obtained the corresponding non-ISA mask layers, labeled as $NISA\text{-}NTL_i$ and $NISA\text{-}GID_i$. Afterwards, we determined whether the two mask layers completely cover the grid cell. If so, the ISA pixels within the grid were considered commissions. Otherwise, the grid was further segmented, i.e., a grid was divided into four sub-grids, and commission identification was subsequently performed on these sub-grids. This process is repeated until the grids are segmented into the size of S. In this study, we set S to 0.0015625° (about 174 m) and its parameter sensitivity was analyzed in Section 5.2.

Finally, based on the identified commissions in the previous step, we created a global commission mask (called GFAM) used to remove commission errors from GISA. The identified commissions were derived from the 2021 potential commissions regions (see Section 3.1). According to the widely accepted assumption that the transition from non-ISA to ISA is typically irreversible (Li et al., 2015), they can be used to eliminate commissions in maps from all the previous years in GISA. In detail, if an ISA pixel in GISA was located within the GFAM, it was relabeled as non-ISA; otherwise, it remained unchanged.

**Algorithm 1** Multi-scale iterative algorithm for commission identification
**Input:** Initial grids with 0.1° $G$, potential commission regions *PFA*, initial mask layers *NISA-GID* and *NISA-NTL*.
**Output:** The identified commissions, *FA*.
1: **for** m = 1 to 7 **do**
2: Compute the total number of grids $N$ in $G$.
3: **for** i = 1 to $N$ **do**
4: Obtain potential commissions $PFA_i$ in $G_i$.
5: Obtain initial mask layers $NISA\text{-}GID_i$ and $NISA\text{-}NTL_i$ corresponding to $G_i$.
6: Determine whether the $NISA\text{-}GID_i$ and $NISA\text{-}NTL_i$ completely cover the grid cell $G_i$.
7: **if** yes **then**
8: Identify $PFA_i$ as commissions.
9: Set the attribute of $G_i$ to 1.
10: **else**
11: Set the attribute of $G_i$ to 1.
12: **end if**
13: **end for**
14: Select the grids with attribute 1 into $G_{FA}$ set // $G_{FA}$ denotes grids with commissions.
15: Obtain identified commissions $FA_m$ using $G_{FA}$
16: Select the grids with attribute 0 into $G_{NFA}$ set // $G_{NFA}$ denotes grids without commissions.
17: Segment $G_{NFA}$, i.e., a grid is divide into 4 sub-grids.
18: Update grids $G$ with $G_{NFA}$.
19: **end for**
20: **Return** The union of { $FA_1$, $FA_2$, ……., $FA_7$}

### 3.4. Accuracy assessment

In this study, we generated a new 30 m global long time-series ISA dataset from 1985 to 2021 (namely GISA-new) by addressing the global omission and commission issues. To validate the effectiveness of the proposed method, we collected two independent test sets to evaluate GISA-new and compared it with existing 30 m global long-time-series ISA datasets, including GISA, GAIA, GAUD, and WSF-evo.

The first test set is the visually interpreted samples derived from historical Landsat imagery, Google Earth imagery, and Landsat NDVI time series. The test set is available every five years, including 1985, 1990, 1995, 2000, 2005, 2010, 2015, and 2018. According to the suggestion of Stehman and Foody (2019), we adopted a cluster sampling strategy to collect samples. Specifically, for each period, we randomly selected 34 grid cells, each with a size of 100 km, at a global scale. For each grid cell, we randomly collected test sample points. Each sample point was manually interpreted by referring to Landsat NDVI time series, Landsat imagery, and Google Earth imagery. In detail, when Google Earth imagery was available, we relied on the information from these high-resolution images to interpret the labels of sample points. When Google Earth imagery was unavailable (e.g., before 2000), sample interpretation using only Landsat imagery may introduce uncertainty owing to its lower spatial resolution (Fig. 6(b)). Therefore, we further utilized the Landsat NDVI time series to examine the sample points (change or unchanged) and interpreted them in combination with later Google Earth imagery. As demonstrated in Fig. 6, the Landsat NDVI time series of the sample point is stable, reflecting no change during the time series (Fig. 6(a)). Thus, the later Google Earth imagery was used to assign the label of the sample point as ISA (Fig. 6(c)). It is worth noting that when the information provided by the Landsat NDVI time series, Landsat imagery, and Google Earth imagery was insufficient or

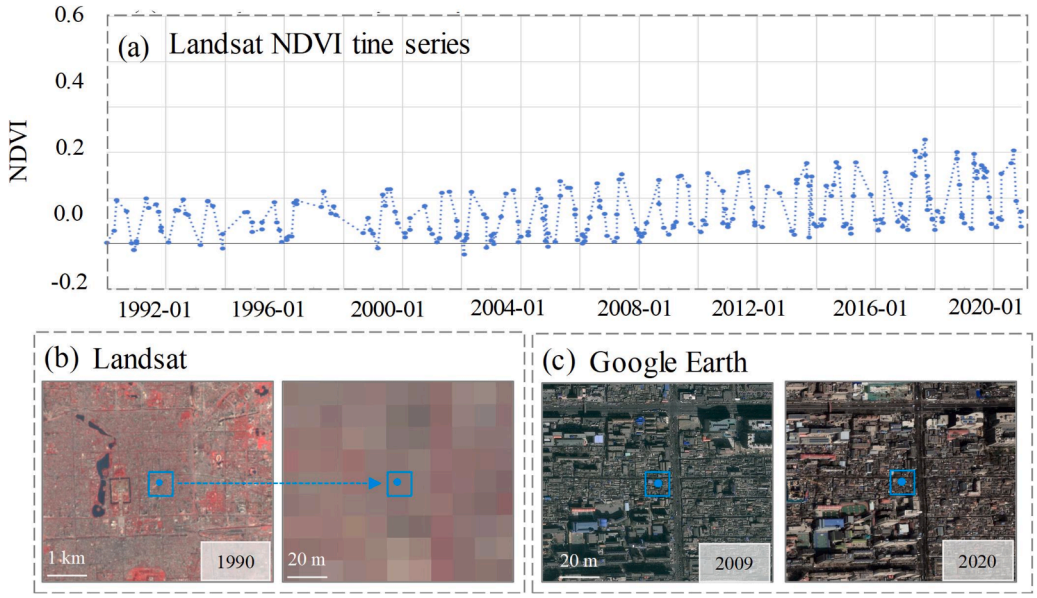


**Fig. 6.** Example of interpreting the validation samples in 1990 using multiple remote sensing imagery, including Landsat NDVI time series, Landsat images, and Google Earth images. The sample point is located at 39.919203°N, 116.402068°E.

uncertain, the sample point was discarded, and another random sample point was chosen. For each grid, the number of ISA samples and non-ISA samples is equal, i.e., 100, to reduce bias in accuracy assessments (Stehman and Foody, 2019). Together, we selected 272 grid cells, totaling 54,400 test samples.

Fig. 7 displays the spatial distribution of test samples. The inset at the bottom represents the number of ISA samples in different ISA density intervals for each year. It can be observed that the ISA test samples are distributed evenly across various ISA density intervals. In this study, a confusion matrix was used to evaluate the accuracy of the global ISA dataset. The accuracy scores include overall accuracy (OA), F1-score, producer's accuracy (PA), and user's accuracy (UA). Since ISA omission and commission errors tend to occur in arid and rural regions (Huang et al., 2022), special attention was paid to the accuracy in these regions. In this study, the arid and rural areas were delineated using urban boundary data (Li et al., 2020) and biomes data (Olson et al., 2001), respectively.

The second test set is the ZY-3 test samples. The test samples were derived from a global built-up area dataset generated from high-resolution and multi-angle ZY-3 remote sensing imagery, covering 45 global cities. The built-up area dataset was generated using multi-angle stereo features, with high spatial resolution (2 m) and high overall accuracy (>90 %) (Liu et al., 2019). Based on the built-up area dataset, we generated ZY-3 test samples for the years 2012–2015. Specifically, for each city, we generated test sample points by randomly sampling within the built-up extent. The number of ISA samples and non-ISA samples is proportional to the area of the built-up area in the city. Then, we labeled the sample points according to ZY-3 imagery. ISA samples are those points with a built-up area proportion greater than or equal to 50 % within a 30 m × 30 m range, while non-ISA samples are those with entirely non-built-up backgrounds within the same range. In total, 60,398 test sample points were collected (Fig. 7).

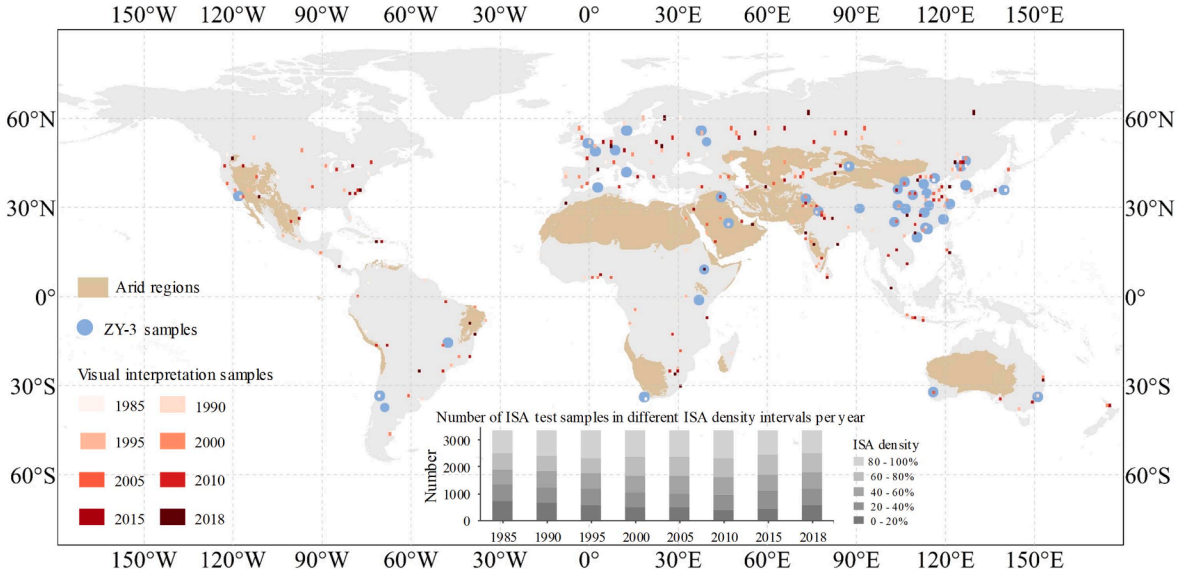


**Fig. 7.** The spatial distribution of the test samples. The inner graph displays the number of ISA test samples in different ISA densities from 1985 to 2018. The ISA density was calculated within the 500 m buffer of the GISA 2021 result.

## 4. Results

### 4.1. Accuracy assessment using visually interpreted samples

#### 4.1.1. Global scale

In this study, a new 30 m global long time-series ISA dataset (GISA-new) was generated (Fig. 8). Based on the visually interpreted samples, we assessed the GISA-new at a global scale. As shown in Fig. 9, the accuracy of GISA-new is promising, with an OA of 93.12 %, which is better than GISA (88.10 %), WSF-evo (91.00 %), GAIA (76.78 %), and GAUD (81.51 %) (Fig. 9(a)). Meanwhile, the F1-score of GISA-new is 0.929, representing an increase of 0.083, 0.023, 0.216, and 0.146 compared to GISA, WSF-evo, GAIA, and GAUD, respectively (Fig. 9(b)), indicating that GISA-new has better performance to detect global ISA. Taking a closer look at the PA and UA, GISA-new has the highest PA (89.50 %), indicating that it suffers less from ISA omissions. Moreover, GISA-new has the highest UA (96.48 %), suggesting a smaller commission error. These quantitative results demonstrate that the proposed methods effectively reduced omission and commission errors in global impervious surface mapping. However, in view of the increase in PA and UA of GISA-new, the former is larger than the latter. For instance, compared to GISA, GISA-new has a 13.51 % increase in PA and a 1.04 % increase in UA. To some extent, this indicates that omissions are more prevailing than commissions in the 30 m global long time-series ISA dataset (Fig. 22).

In terms of the accuracy in different years, GISA-new also obtains the highest OA and F1-score (Fig. 10(a)-(b)). Note that the accuracy of the global ISA datasets varies in years. For example, the OA of GISA-new ranges from 89.91 % to 95.22 %, and the F1-score ranges from 0.891 to 0.951. However, GISA-new has a smaller accuracy variance, with an OA variance of 1.7 % and an F1-score variance of 0.018, which are lower than the accuracy variance of WSF-evo (2.3 %, 0.027), GISA (1.7 %, 0.022), GAIA (5.3 %, 0.095), and GAUD (2.8 %, 0.037) (Fig. 10(c)-(d)). This indicates that GISA-new exhibits a stable performance across years, probably because the proposed method of this study reduced the ISA omissions and commissions in different periods.

To validate the above observations, taking typical omission and commission errors (i.e., rural areas, and water bodies) as examples, the results of the global ISA dataset in an early period (i.e., 1985) and a later period (i.e., 2015) were displayed. As shown in Fig. 11(a), GISA-new detects more ISA in different years, while other global ISA datasets (e.g., GISA, WSF-evo, GAIA, and GAUD) suffer from omissions, especially in 1985. As for Fig. 11(b), other global ISA datasets present commission errors caused by water bodies. These errors accumulate over time in GISA and GAIA. On the contrary, GISA-new classifies water bodies as non-ISA throughput the years.

#### 4.1.2. Regional scale

Fig. 12 displays the accuracy of the global ISA datasets in different regions, including arid and non-arid regions, and rural and urban regions. Similar to the global results, GISA-new is superior to the other datasets, i.e., GISA, WSF-evo, GAIA, and GAUD. However, the accuracy gap between GISA-new and the other datasets is greater in arid and rural areas. Specifically, compared to GISA, GISA-new increases OA by 10.9 % and 8.0 % in arid and rural regions, respectively, while the OA increases by 6.1 % and 4.8 % in non-arid and urban regions, respectively (Fig. 12 (a)). The phenomenon is also observed in other accuracy scores, e.g., F1-score, UA, and PA (Fig. 12(b)-(d)).

Moreover, we investigated the accuracy of global ISA datasets in arid and rural regions for different years. It can be seen that GISA-new presents higher and more constant time-series accuracy. For example, in the rural areas, the OA of GISA-new is above 89 % with a variance of 1.6 %; in arid regions, the OA of GISA-new exceeds 86 %, with a variance of 2.6 %. As regards the other datasets (i.e., GISA, WSF-evo, GAIA, and GAUD), their accuracy is relatively lower and unstable. Taking GAUD as an example, its OA is more than 76 % with a variance of 2.5 % in the rural regions, and 63 % with a variance of 4.7 % in the arid areas. This may be due to the lower performance of GAUD before 2000 (Fig. 13(c), (f)).

### 4.2. Accuracy assessment using ZY-3 test samples

Based on ZY-3 test samples, we further evaluated the global ISA datasets. As shown in Table 2, GISA-new reaches the highest accuracy, with an OA of 91.85 % and an Kappa of 0.827, followed by WSF-evo (91.17 %, 0.813), GISA (90.18 %, 0.786), GAUD (90.81, 0.802), and GAIA (88.73 %, 0.756). It should be noted that the ZY-3 test samples tend to reflect the accuracy in urban areas, as the ZY-3 built-up area dataset covered representative global cities (Liu et al., 2019). As a result, there is less difference in accuracy among these global ISA datasets.

## 5. Discussions

### 5.1. The effect of the auxiliary datasets

In this study, the influence of the WSF 2019, ESA, and NTL on the proposed method was investigated.

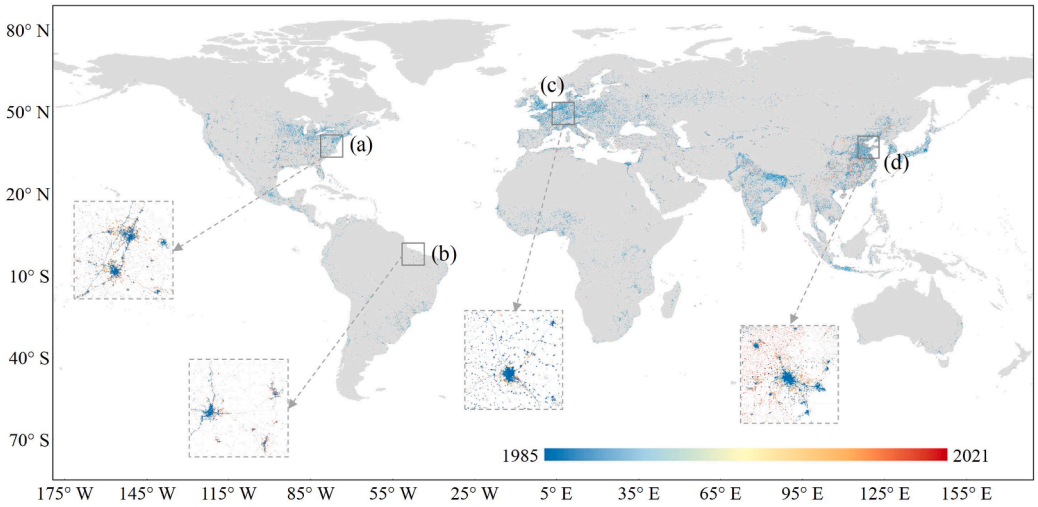


**Fig. 8.** ISA dynamics from 1985 to 2021 at the global scale. (a), (b), (c), and (d) represent representation regions in North America, South America, Europe, and Asia, respectively.

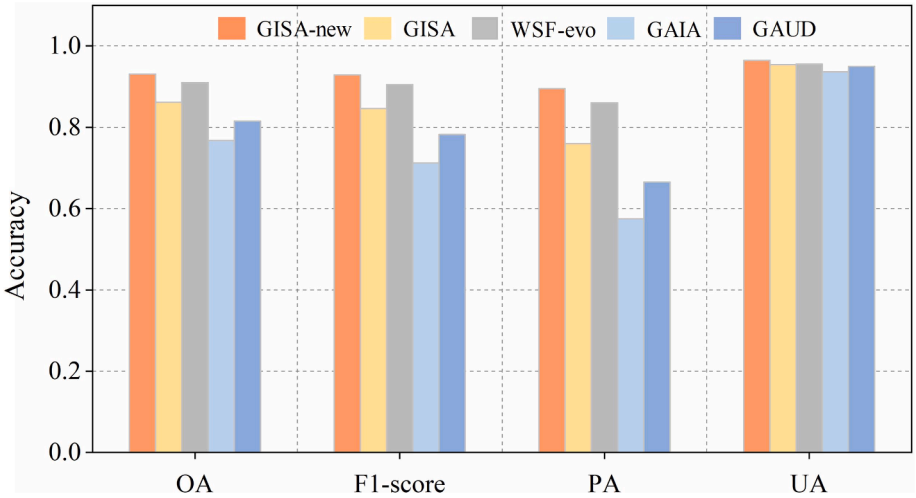


**Fig. 9.** Accuracy assessment of GISA-new and existing datasets at a global scale obtained using visual interpretation samples. (a) OA. (b) F1-score of ISA. (c) PA. (d) UA.

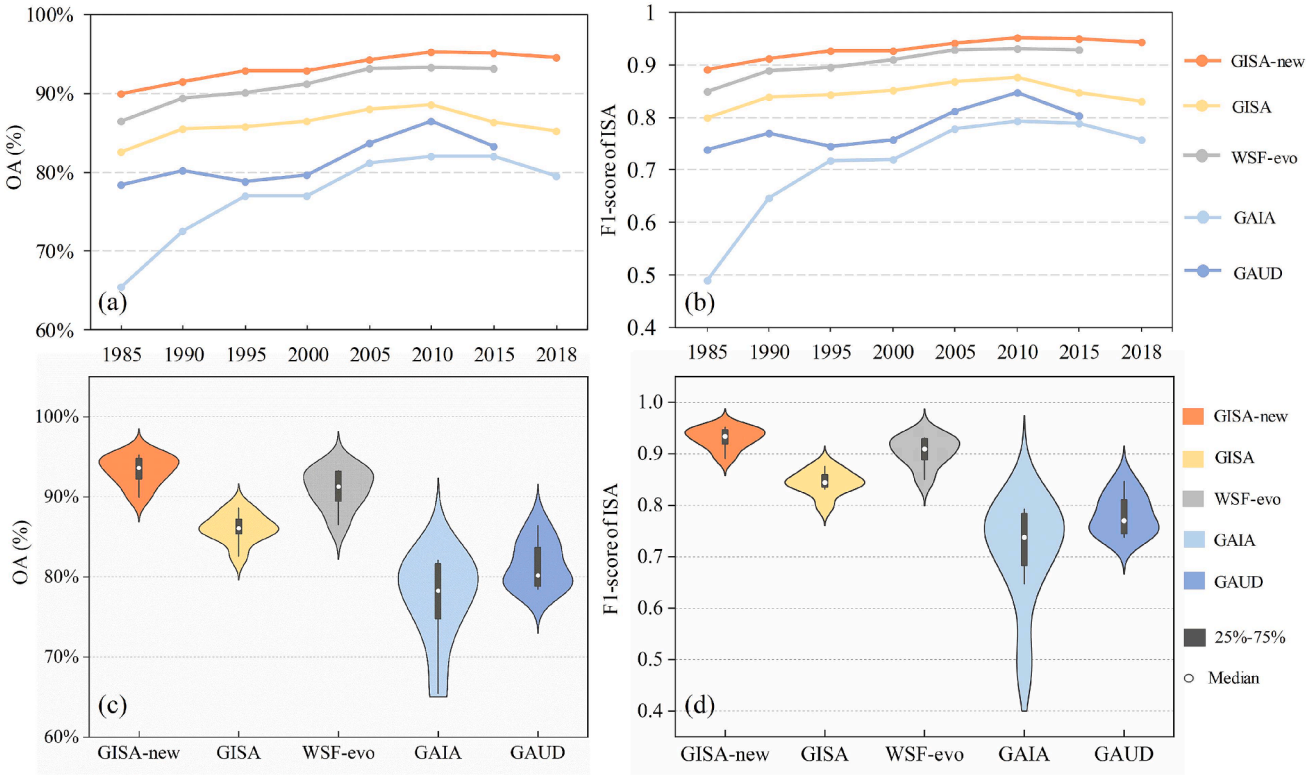


**Fig. 10.** Accuracy of GISA-new and existing global-scale datasets for different years. (a) and (b) represent the OA and F1-score of ISA at different time periods, respectively. (c) and (d) represent the violin plot of OA and F1-score of ISA, respectively.

### 5.1.1. *Effect of the WSF and EAS datasets*

In this study, to reduce the uncertainties in the global ISA mapping, potential omission and commission regions were generated by using WSF 2019 and ESA. To evaluate their effectiveness, we conducted additional experiments. Table 3 shows that the accuracy is lower when using only WSF 2019 or ESA dataset, and their combination yields higher accuracy. OA increased by 1.22 % and 0.15 % compared to using WSF 2019 or ESA alone, respectively. These results indicate that their combined use facilitates more accurate global ISA mapping.

### 5.1.2. *Effect of building footprints in reducing ISA omissions*

To further reduce global ISA omission, the large-scale building footprint datasets, including Microsoft's building footprint (Microsoft, 2022) and vectorized rooftop area data for 90 cities in China (Zhang et al., 2022b), were also incorporated as potential omission regions (Section 3.1.1).

As shown in Table 4, incorporating building footprints resulted in an increase of 1 % in OA, 2 % in Kappa, 1 % in F1-score of ISA, and 1 % in F1-score of NISA, demonstrating the effectiveness of building footprints in reducing ISA omissions. In addition to the quantitative results, visual comparisons reinforced the conclusion. As illustrated in Fig. 14, the inclusion of building footprints can identify the scattered and small ISAs in low-density regions, showcasing its superiority in capturing detailed information. Specifically, in site 1, ISA objects along the urban boundary

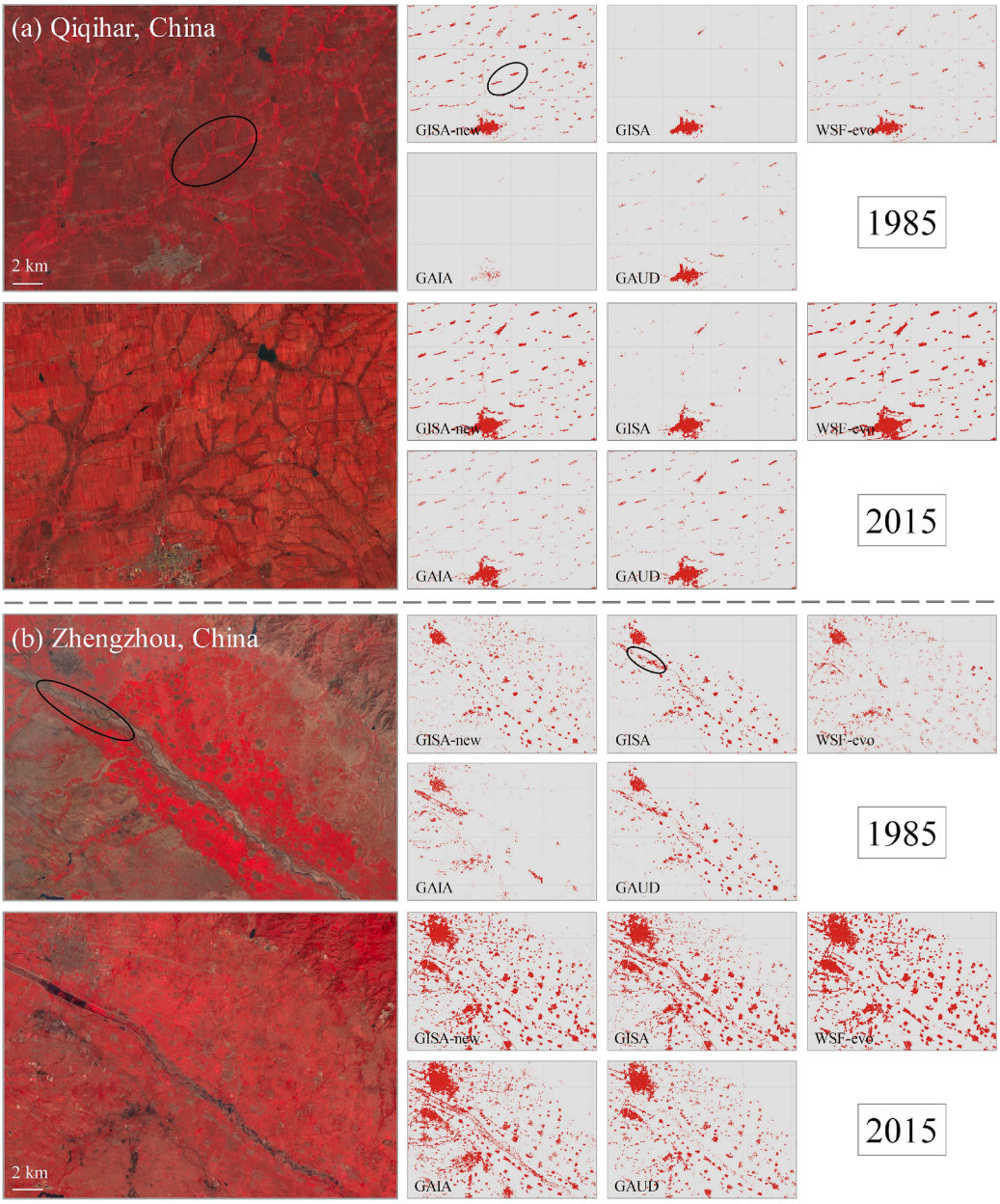


**Fig. 11.** Comparison of GISA-new and existing global ISA datasets at two representative omission and commission regions in 1985 and 2015. (a) omission regions. (b) commission regions. The Landsat imagery is composited in a false-color combination (R: NIR, G: red, B: green). (For interpretation of the references to color in this figure legend, the reader is referred to the web version of this article.)

were detected, and in site 2, ISAs were captured more completely. However, these regions were not effectively detected in the results of WSF 2019 and ESA.

#### 5.1.3. *Effect of non-ISA mask in the MIA algorithm*

To investigate the impact of the auxiliary datasets (including WSF 2019, ESA, and NTL) on the MIA algorithm, we performed a comparative experiment. In detail, three non-ISA masks were compared: NISA-NTL, NISA-GID, and combination of NISA-NTL and NISA-GID. Results are presented in Table 5, where it can be seen that the lowest accuracy was achieved with the NISA-NTL mask alone. NTL has limited ability of identifying the potential commission regions since it shows weak light for some roads or small targets. Accuracy was improved using the NISA-GID mask, with increases of OA and F1-score by 1.20 % and 0.012, respectively, attributed to the high accuracy of the 10 m global ISA dataset. The combined use of NISA-NTL and NISA-GID masks led to the highest accuracy, demonstrating that the integration of WSF 2019, ESA and NTL is more effective in removing global commissions.

### 5.2. *Performance of NA-CCDC*

In response to global ISA omissions, we proposed a multi-temporal CCDC algorithm that accounts for newly added ISA areas (NA-CCDC). This method incorporated multi-temporal and newly added ISA region (NIR) sampling to enhance the ability of the CCDC algorithm to detect ISA. To validate the performance of NA-CCDC, we compared it with the original CCDC algorithm (i.e., with training samples from a single year) and the multi-temporal CCDC algorithm (i.e., with training samples from multiple years, written as MT-CCDC). For the original CCDC, by referring to Xie et al. (2022), the samples were extracted from the 2000 ISA sample pool (Section 3.2.1) as it is close to the center of the mapping periods (i.e., 1985–2021) of this study. The MT-CCDC, on the other

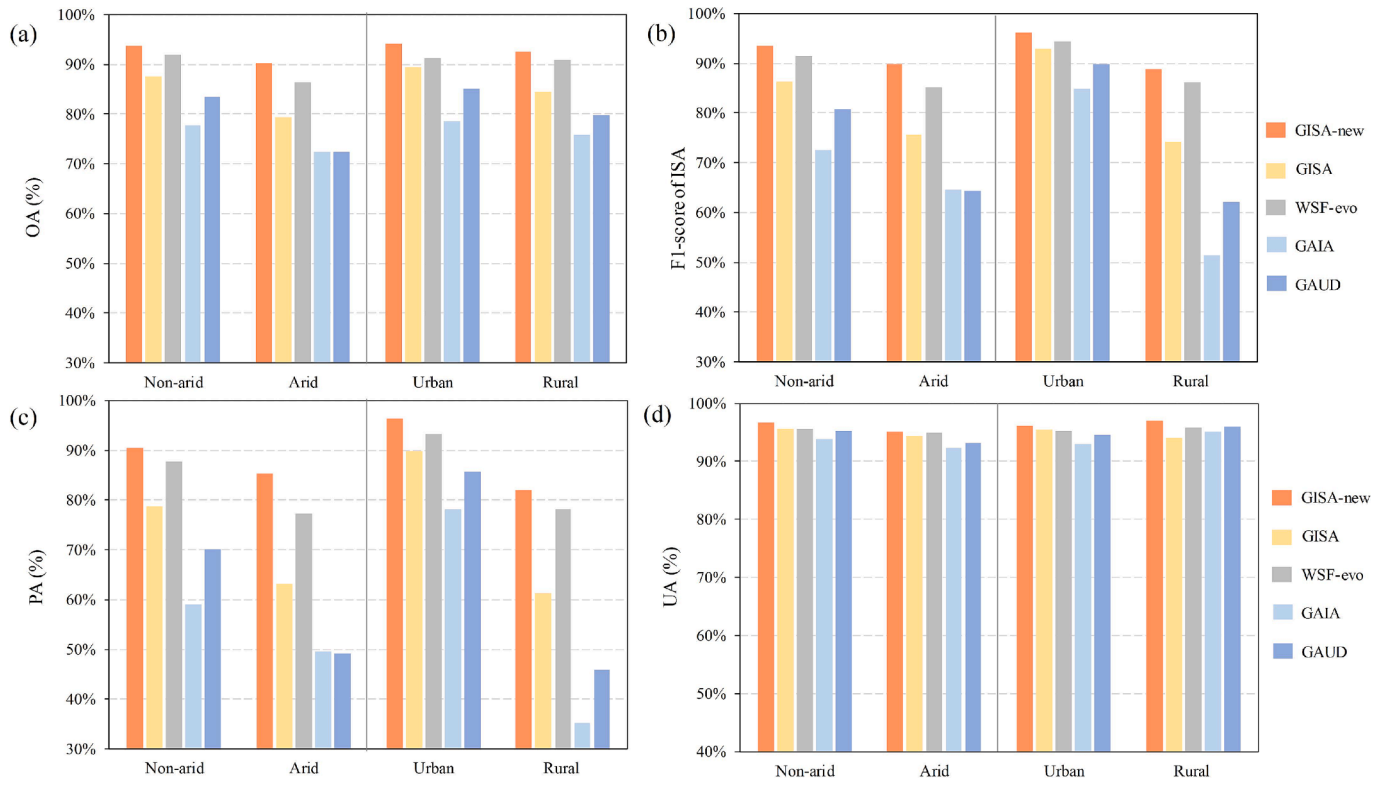


**Fig. 12.** Accuracy assessment of GISA-new and existing datasets at regional scale obtained using visual interpretation samples. (a) OA. (b) F1-score of ISA. (c) PA. (d) UA.


**Fig. 13.** Accuracy of GISA-new and existing global-scale datasets for different time periods in arid and rural regions. (a) and (d) represent the OA and F1-score of ISA for different time periods in arid regions, respectively. (b) and (e) represent the OA and F1-score of ISA for different time periods in rural regions, respectively. (c) represents the violin plot of OA in arid and rural regions. (d) represents the violin plot of the F1-score of ISA in arid and rural regions.

hand, used multi-year samples as input data (Wang et al., 2024). The samples were randomly collected from the ISA sampling pools in 1990, 2000, 2010, and 2020, respectively. Notice that compared to NA-CCDC, the MT-CCDC selected time-series samples but did not lay stress on the newly added ISA regions.

At the global scale, we randomly selected 10 grid cells as test regions. To ensure a fair comparison, the number of training samples and the classification parameters were kept the same for different methods (see Section 3.2.2). In addition, for a quantitative assessment, we employed stratified random sampling to collect validation data. Specifically, for each test grid, we randomly selected 100 samples. Afterwards, following the same manner (see Section 3.4), we manually interpreted the land cover types of these samples (i.e., ISA or non-ISA) at 5-year intervals from 1985 to 2020. In total, 1000 test samples were used for accuracy assessment in this section. Fig. 15 shows the accuracy of different methods. It can be seen that the CCDC obtained the lowest accuracy,

**Table 2**
Results of accuracy assessment via ZY-3 test samples between GISA-new and existing time-series ISA datasets. OA represents overall accuracy.

| Global | OA (%) | Kappa | F1-score of ISA | F1-score of non-ISA | PA (%) | UA (%) |
|---|---|---|---|---|---|---|
| GISA-new | 91.85 | 0.827 | 0.892 | 0.934 | 92.54 | 86.14 |
| WSF-evo | 91.17 | 0.813 | 0.885 | 0.929 | 92.76 | 84.54 |
| GISA | 90.18 | 0.786 | 0.862 | 0.924 | 83.75 | 88.71 |
| GAIA | 88.73 | 0.756 | 0.844 | 0.912 | 83.78 | 82.11 |
| GAUD | 90.81 | 0.802 | 0.875 | 0.927 | 88.13 | 86.88 |

**Table 3**
Effect of the WSF and ESA datasets, where the best values of each metric are highlighted in bold.

| Dataset used | OA (%) | Kappa | F1-score of ISA | F1-score of NISA |
|---|---|---|---|---|
| WSF 2019 | 91.02 | 0.824 | 0.906 | 0.917 |
| ESA | 92.09 | 0.842 | 0.917 | 0.925 |
| WSF 2019 and ESA | **92.24** | **0.845** | **0.918** | **0.926** |

**Table 4**
Accuracy comparison with and without building footprints.

| Building footprints | OA (%) | Kappa | F1-score of ISA | F1-score of NISA |
|---|---|---|---|---|
| Without | 92.24 % | 0.845 | 0.918 | 0.926 |
| With | 93.29 % | 0.866 | 0.930 | 0.935 |

with a mean OA of 84.33 % (Fig. 15(b)). The MT-CCDC achieved a mean OA increase of 1.7 %. This suggests that using ISA information from multiple years can enhance the classification results generated by CCDC. The proposed NA-CCDC achieved the best accuracy, with a mean OA of 87.24 %, verifying that ISA information in changed areas contributes to detecting ISA and reducing omissions in the global scale.

Fig. 15(a) shows the difference in accuracy among various methods for different years. It can be found that the accuracy of the NA-CCDC exhibits a noticeable increasing trend after 2000, outperforming the MT-CCDC, which does not consider newly added ISA areas. This phenomenon verifies the reasonableness of the NA-CCDC, as ISA expansion accelerated rapidly after 2000. Taking Yinchuan, China, as an example, we visualized the classification results of different methods. As shown in Fig. 16, the CCDC demonstrates a poor ability to identify newly added ISAs (Fig. 16(a)), while the MT-CCDC can identify newly added ISA targets but not precisely enough. In contrast, the NA-CCDC more completely detected ISAs owing to ISA sample collection in changed areas (Fig. 16 (b)), validating the effectiveness and necessity of incorporating information from newly added ISA areas for global ISA monitoring.

### 5.3. Effect of MIA method for commissions removal

To address the issue of commissions, we proposed a multi-scale iterative (MIA) method. This method conducted an iteration operation on grids of varying scales to automatically identify and remove commissions on a global scale. First, we discussed the effect of the termination conditions. In detail, we randomly selected 50 grid cells with 0.1° sides across the globe as test regions. The accuracy of commission identification was calculated using grids of different scales as termination conditions, including 11132 m (0.1°), 5566 m (0.05°), 2783 m (0.025°), 1392 m (0.0125°), 696 m (0.00625°), 348 m (0.003125°), 174 m (0.0015625°), 86 m (0.00078125°), and 43 m (0.000390625°). The results are depicted in Fig. 17. It can be observed that as the number of iterations increases, the accuracy shows an upward trend. This indicates that the iterative strategy is beneficial for identifying ISA commissions. Notably, when the number of iterations reaches 7, corresponding to a grid cell size of 174 m, the accuracy gain starts to slow down and even slightly decreases. Additionally, smaller grid cells require more computational resources. Therefore, we selected a grid of 174 m as the termination condition of this study.

**Table 5**
Accuracies with different non-ISA masks used to identify potential commission regions, where the best values of each metric are highlighted in bold. NISA-NTL represents the non-ISA mask derived from NTL data, and NISA-GID represents the non-ISA mask derived from WSF 2019 and ESA.

| Non-ISA mask | OA (%) | Kappa | F1-score of ISA | F1-score of NISA |
|---|---|---|---|---|
| *NISA-NTL* | 91.10 | 0.822 | 0.907 | 0.915 |
| *NISA-GID* | 92.30 | 0.846 | 0.919 | 0.927 |
| *NISA-NTL & NISA-GID* | **92.60** | **0.852** | **0.925** | **0.927** |

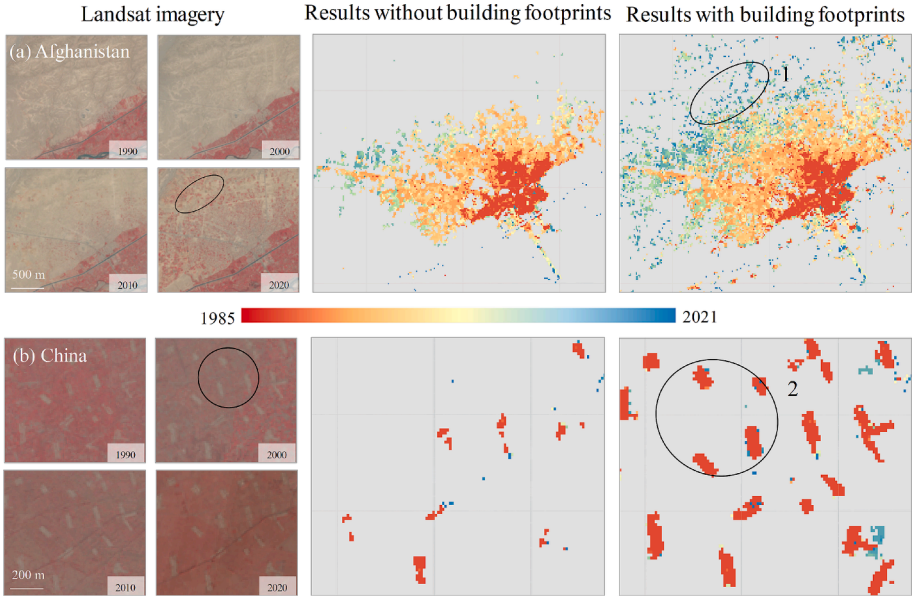


**Fig. 14.** Examples of the ISA detection with and without consideration of global building footprints. Landsat imagery is composited by NIR, red, and green channels. (For interpretation of the references to color in this figure legend, the reader is referred to the web version of this article.)

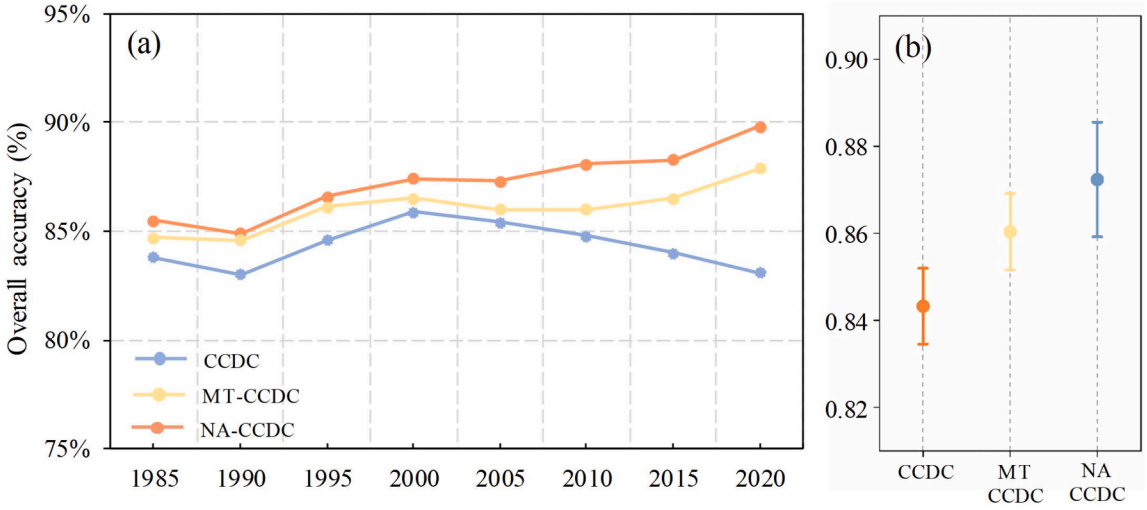


**Fig. 15.** Accuracies obtained from CCDC, MT-CCDC and NA-CCDC. (a) represents the accuracy of different time periods. (b) represents the interval plot of accuracy for different periods. MT-CCDC: Multiple temporal CCDC; NA-CCDC: Newly added ISA regions CCDC.

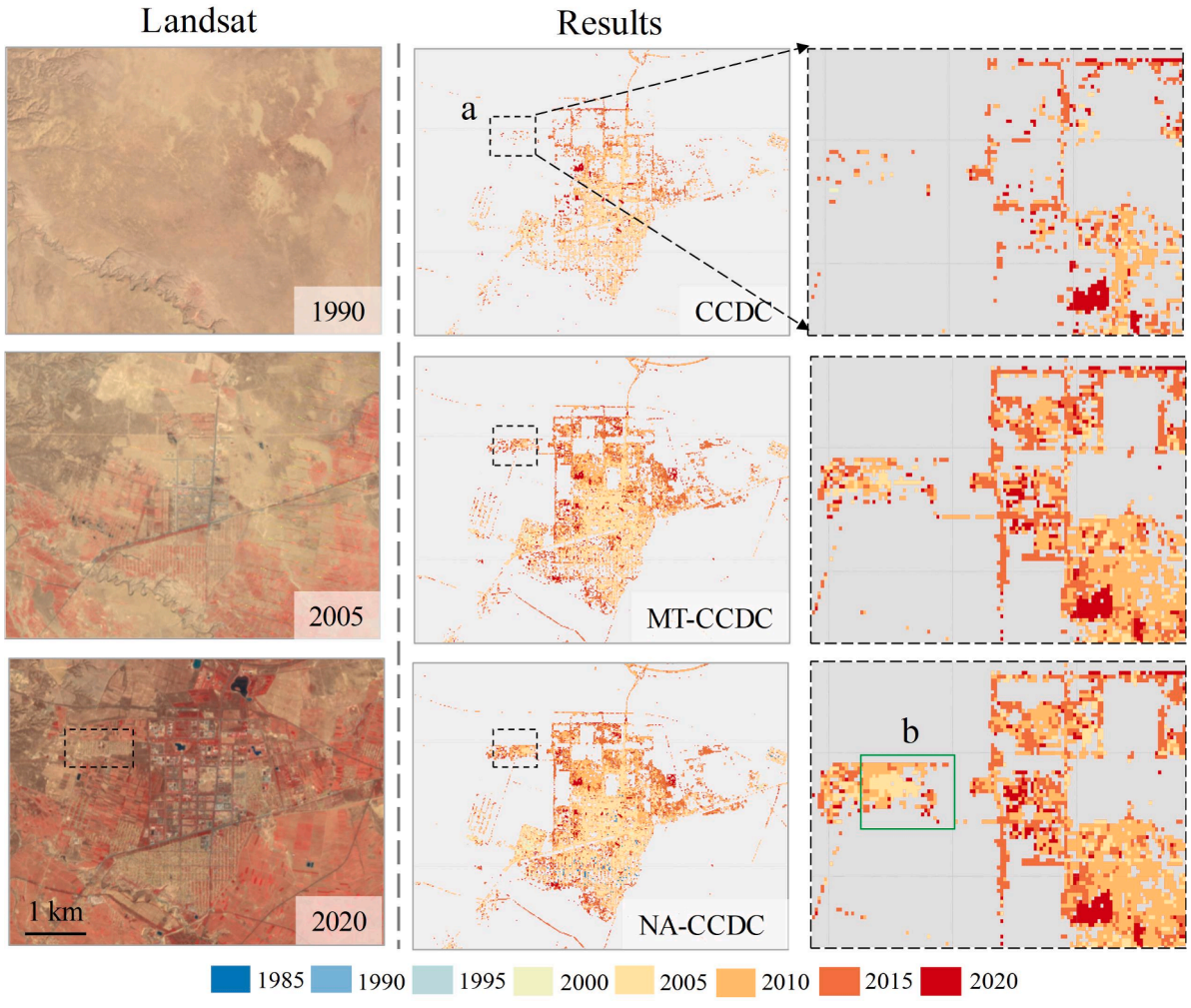


**Fig. 16.** An example of time-series ISA omission filling for different methods. Landsat imagery, which is composited by B5, B4, and B3 in the NIR, red, and green channels. MT-CCDC: Multiple temporal CCDC; NA-CCDC: Newly added ISA regions CCDC. (For interpretation of the references to color in this figure legend, the reader is referred to the web version of this article.)

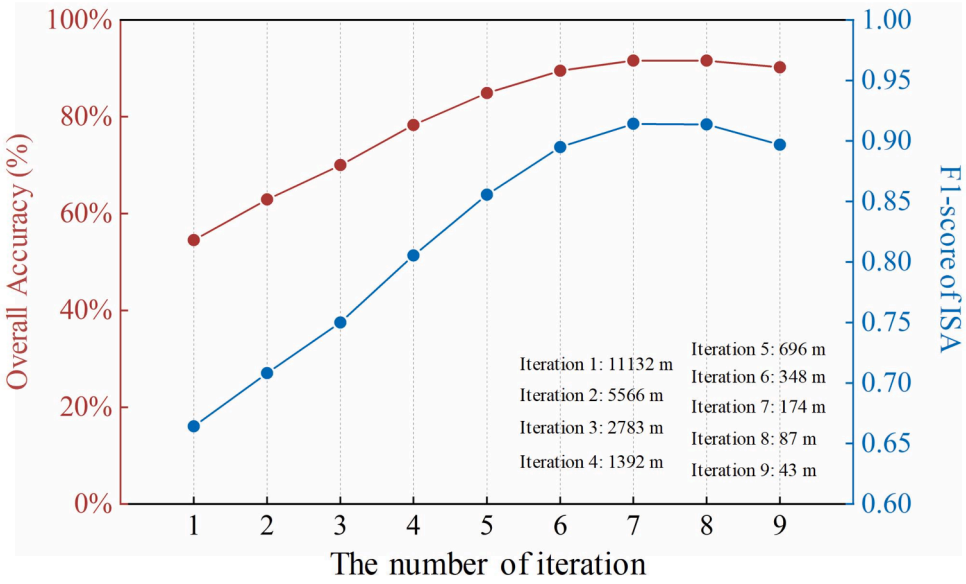


**Fig. 17.** Quantitative performance analysis with the different number of iterations in commission identification.

To illustrate the performance of the MIA method for commission identification, we visualized the identification process and compared it with the pixel-based commission identification. The pixel-based method defines ISAs corresponding to the non-ISA pixels in a mask layer as commissions. Specifically, ISAs are identified as commissions when both mask layers (i.e., *NISA-GID* and *NISA-NTL*) show non-ISA at the pixel level. Taking two typical commission regions, i.e., bare soil and water bodies, as examples, the results are shown in Fig. 18.

In general, the proposed MIA method demonstrated more accurate results in identifying commissions. Specifically, in the example of Xiangyang, China (Fig. 18(a)), bare soil resulted in a large number of commissions of various sizes. It can be seen that these commissions are successively identified by the iterative strategy. In the example of Multan, Pakistan (Fig. 18(b)), extensive water bodies were misclassified as ISAs. However, these commissions are close to residential areas, complicating their detection. For instance, when the grid cell is large, the non-ISA mask may cover residential areas, failing to meet the commission identification criteria (i.e., both non-ISA masks cover the entire grid cell simultaneously). As a result, from iterations 1 to 4, commissions were not identified. As the iteration process continued, the grid gradually became smaller and satisfied the identification criteria, thus commissions were identified. Both examples demonstrate the effectiveness of commission identification using a grid-based multi-scale iterative strategy. By contrast, the pixel-based method misidentified true ISA information as commissions, such as roads (region 1) in example (a) and buildings (region 2) in example (b). However, these elements can be accurately separated from commissions using the proposed MIA method.

Fig. 19 shows the efficacy of the MIA method for commission removal across different years. In this study, two examples were selected to visually compare the results before and after commission removal over four years: 1990, 2000, 2010, and 2020. Specifically, in the case of Fig. 19(a), commissions caused by mining areas first appeared on the 2000 map and accumulated in subsequent years, e.g., 2010 and 2020. Based on the proposed MIA method in this study, commissions on the 2000, 2010, and 2020 maps were successfully removed. In the case of Fig. 19(b), commissions caused by water bodies only existed on the 2020 map and were also removed.

### 5.4. Effect of the classification features

In this section, we investigate the effect of classification features on global ISA mapping. Referring to existing studies (Zhu and Woodcock, 2014a), the spectral bands (including blue, green, red, near-infrared (NIR), shortwave infrared (SWIR), and thermal infrared (TIR) bands) along with ancillary data (including slope, elevation, and aspect) were used as inputs for NA-CCDC. The multispectral bands are used since they present important properties for land cover classification (e.g., ISA). Meanwhile, temporal information is also an important factor for ISA mapping since ISA usually exhibit less temporal variability compared to the natural land cover. Therefore, in this study, all available Landsat observations from 1985 to 2021 were used. As shown in Fig. 20, within a year, the red and NIR records for non-ISA exhibit significant changes, while the temporal curves for ISA are relatively stable, which aids in distinguishing ISA from non-ISA. Additionally, topographical variables contribute to ISA mapping (Ban et al., 2015; Zhang et al., 2020), especially reducing the confusion between complex terrain and buildings. Consequently, these topographical variables were also used as ancillary data in this study.

To quantitatively assess the effectiveness of the classification features, we conducted ablation experiments. As presented in Table 6, the joint features of spectral and ancillary achieve the best performance, with an OA of 87.24 % and a Kappa of 0.744. The removal of ancillary data resulted in a decrease in accuracy, with a reduction of 0.66 % in OA and 0.014 in Kappa. Moreover, the results show that the exclusion of any individual spectral band led to a decline in accuracy, confirming that the selected classification features in this study are reasonable.

### 5.5. The assumption of ISA irreversibility

Referring to Huang et al. (2021), we implemented the assumption of ISA irreversibility using the spatio-temporal filtering. Specifically, a $3 \times 3 \times 5$ spatio-temporal filter (3 and 5 represent the spatial and temporal window sizes, respectively) is used to refine the time-series ISA maps. To evaluate its influence, we compared the results with and without the spatio-temporal filtering. As shown in Table 7, the filter resulted in a slight accuracy increment, by 0.14 % in OA. This reflects that the influence of the spatio-temporal filtering seems marginal, and the accuracy gains brought by the filtering outweigh the accuracy loss caused by its uncertainties.

### 5.6. Accuracy assessment under different cloud coverage conditions

To investigate the effect of cloud coverage, we compared the accuracy under different cloud cover conditions among the global ISA

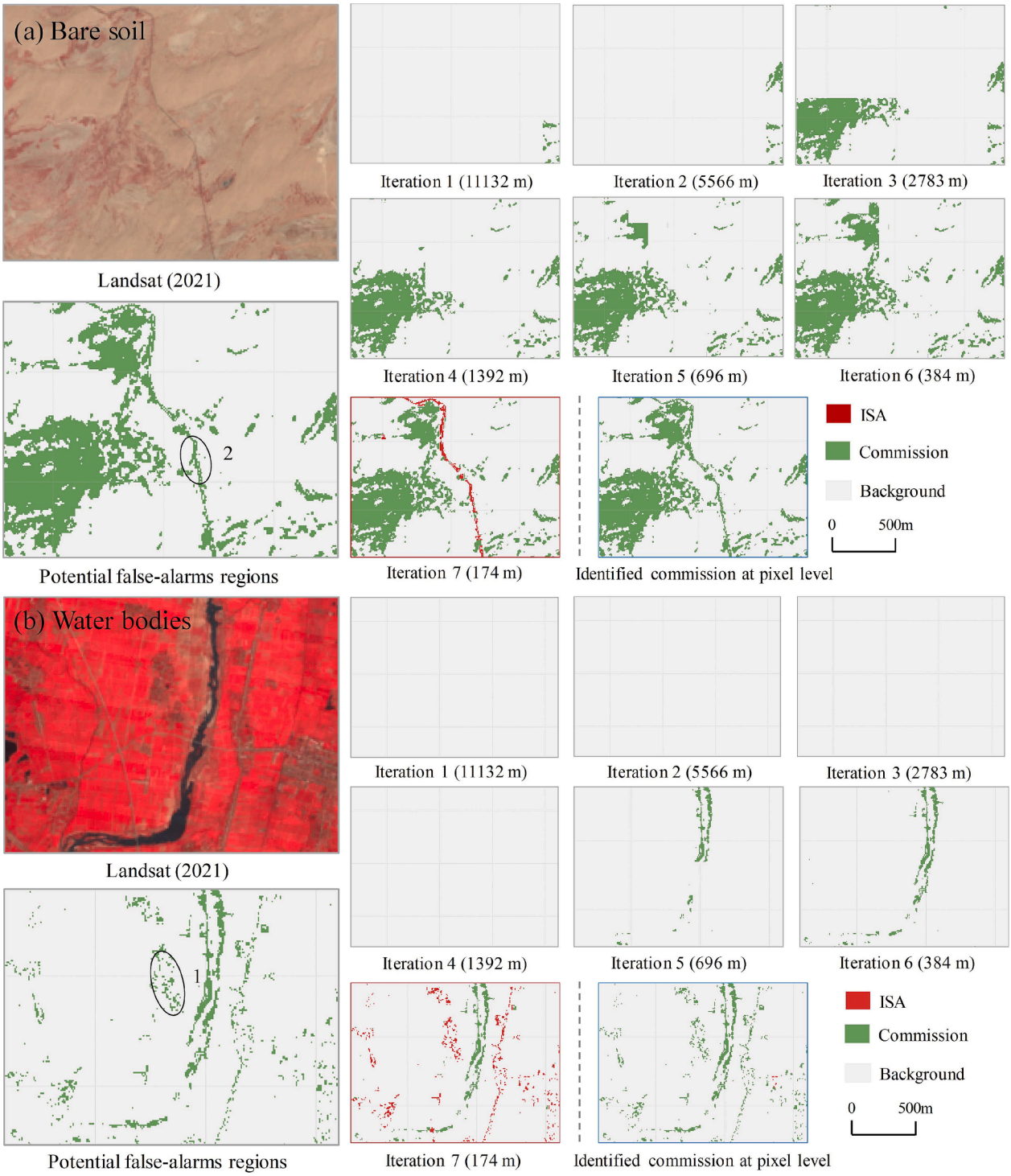


**Fig. 18.** Visualization results of multi-scale iterative commissions removal. (a) represents commissions caused by bare soil in Xiangyang, China; (b) represents commissions caused by water in Multan, Pakistan. The red box represents the final result of the commission identification using a multi-scale iterative method. The blue box represents the result of the commission identification using non-ISA masks at the pixel level. The Landsat imagery is composited by B5, B4, and B3 in the NIR, red, and green channels for 2021. (For interpretation of the references to color in this figure legend, the reader is referred to the web version of this article.)

datasets. The cloud cover percentage was calculated as the frequency of unclear observations (i.e., the number of cloud-covered observations) in all the observations from 1985 to 2021. Here, the visually interpreted samples (Section 3.4) were used as samples. Four cloud coverage levels were used in an interval of 25 %: Level 1 (100 % – 75 %), Level 2 (75 % – 50 %), Level 3 (50 % – 25 %), and Level 4 (25 % – 0 %).

The results are shown in Fig. 21. It can be seen that, compared to other global ISA datasets, GISA-new outperforms across varying cloud coverage, with OA stably exceeding 93 %. Specifically, as cloud coverage decreases, the accuracy of GISA-new exhibits an upward trend. Notably, at Levels 1 and 2, corresponding to higher cloud coverage, the accuracy gap between GISA-new and other datasets is more pronounced, demonstrating the advantage of GISA-new in handling more cloud coverage. In general, these results demonstrate the reliability and stability of GISA-new.

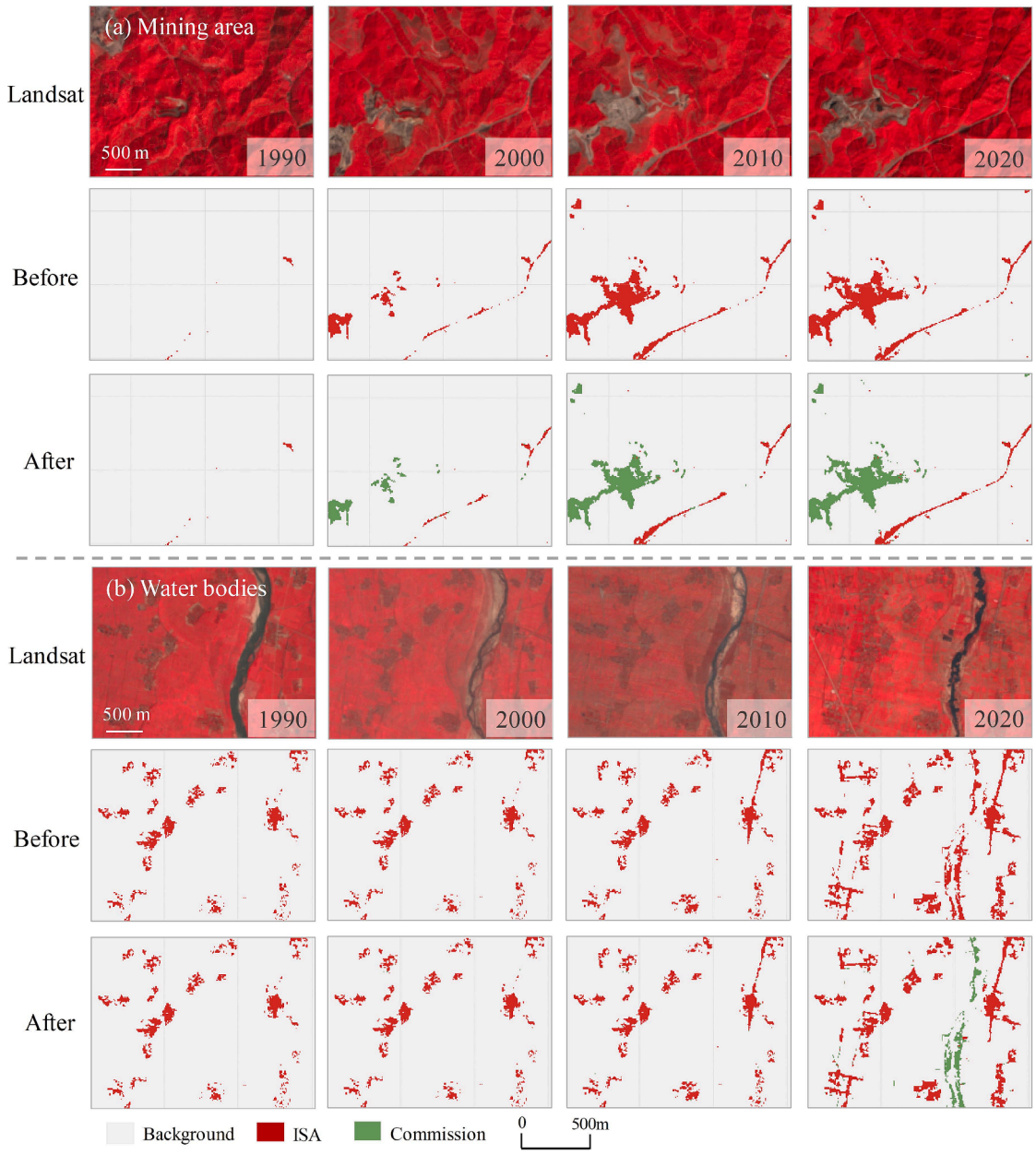


**Fig. 19.** Visualization results before and after commission elimination for different years. The black box represents the commission of ISA. The Landsat imagery is composited by B5, B4, and B3 in the NIR, red, and green channels for 2021. (For interpretation of the references to color in this figure legend, the reader is referred to the web version of this article.)

### *5.7. The analysis of global ISA omissions and commissions*

Based on the proposed method in this study, we addressed the omission and commission errors in the existing global long-term ISA dataset and generated a new global ISA dataset, GISA-new. In this context, we attempted to analyze the spatial distribution of global ISA omissions and commissions between 1985 and 2021. To this end, we first defined the omission rate and commission rate. The omission rate is the percentage of the ISA omission area filled between 1985 and 2021 relative to the total area of the 0.06° grid, while the commission rate is the percentage of the ISA commission area removed between 1985 and 2021 relative to the total area of the 0.06° grid.

As shown in Fig. 22(a), ISA omissions show an extensive distribution. Particularly, the high-density impervious surface areas (see Fig. 8), such as China, India, and Germany, have a higher omission rate due to their complex and diverse background environments. It should be noted that the omission rates of most regions are below 30 %, indicating that omissions are prone to occur in low-density impervious surfaces. An imbalance in the distribution of ISA omissions is found between the Southern and Northern Hemispheres (Fig. 22(b)). Specifically, in the Northern Hemisphere, ISA omissions are concentrated between 10° N ~ 55° N, accounting for 72 % of global ISA omissions. By contrast, the Southern Hemisphere has much fewer ISA omissions, which are distributed evenly between 0∘ S and 50∘ S without distinct area peaks. The possible reason for this discrepancy is that Asia and Europe have more rural ISA (Huang et al., 2022), which is easily omitted.

On the other hand, ISA commissions show a similar distribution pattern to ISA omissions, with more aggregation apparent in Northern Hemisphere countries such as China, Germany, and the United States (Fig. 22(d)). Consequently, commission errors are more severe in the Northern Hemisphere than in the Southern Hemisphere (Fig. 22(e)), accounting for 87 % of the global ISA commissions (Fig. 22(f)).

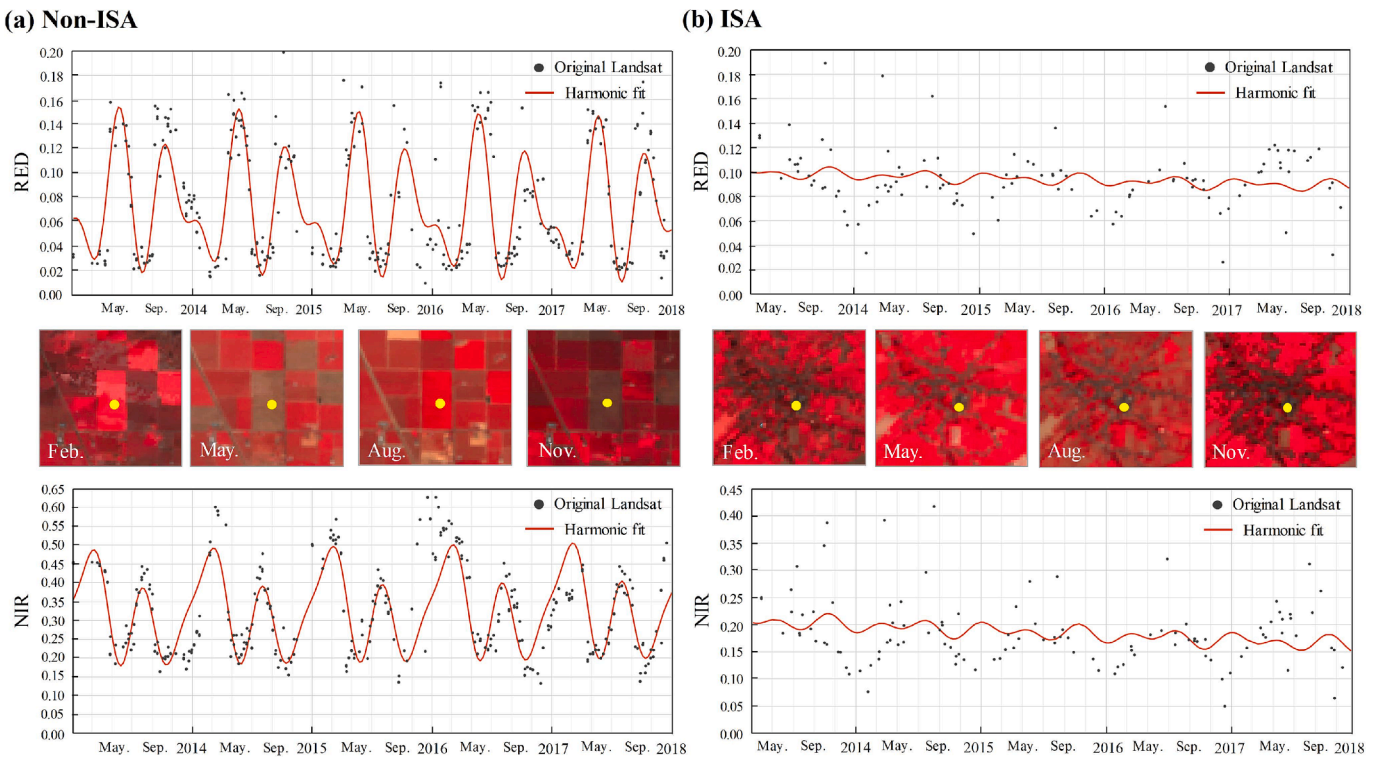


**Fig. 20.** Temporal profiles of non-ISA (a) and ISA (b) from red and NIR bands. Landsat imagery, which is composited by NIR, red, and green channels. (For interpretation of the references to color in this figure legend, the reader is referred to the web version of this article.)

**Table 6**
Accuracy comparison for different feature combinations, where the best values of each metric are highlighted in bold.

| | OA (%) | Kappa | F1-score of ISA | F1-score of NISA |
|---|---|---|---|---|
| Without ancillary | 86.58 % | 0.730 | 0.855 | 0.875 |
| Without blue | 86.94 % | 0.738 | 0.861 | 0.877 |
| Without green | 86.94 % | 0.738 | 0.861 | 0.877 |
| Without red | 86.79 % | 0.735 | 0.860 | 0.875 |
| Without NIR | 86.80 % | 0.735 | 0.860 | 0.875 |
| Without SWIR1 | 86.59 % | 0.731 | 0.858 | 0.873 |
| Without SWIR2 | 86.88 % | 0.737 | 0.861 | 0.876 |
| Without TIR | 86.30 % | 0.725 | 0.854 | 0.871 |
| All features | **87.24 %** | **0.744** | **0.865** | **0.879** |

**Table 7**
Accuracies with and without the assumption of ISA irreversibility, where the best values of each metric are highlighted in bold.

| The assumption of ISA irreversibility | OA (%) | Kappa | F1-score of ISA | F1-score of NISA |
|---|---|---|---|---|
| Without | 93.16 % | 0.863 | 0.929 | 0.934 |
| With | **93.29 %** | **0.866** | **0.930** | **0.935** |

However, the commission rates are less than 10 % in most regions, which is lower than the omission rate (i.e., 30 %). In addition, regarding statistical results, the global ISA omission area is approximately 374,890 $km^2$, while the global ISA commission area is about 4,559 $km^2$. Therefore, omission errors exhibit a greater challenge for accurate global ISA monitoring.

Fig. 23 displays the typical ISA omissions and commissions in various landscapes. As shown in Fig. 23(a)-(c), omissions mainly contain two types: rural omissions and suburban omissions. The rural omissions present spatial aggregations in eastern China, Japan, and Uzbekistan (Fig. 22(a)), attributed to the fact that there are more rural ISAs in these regions. As for suburban omissions, clusters are commonly found in North America (Fig. 23(d)). These omission errors lead to underestimations of ISA (Huang et al., 2022; Pasquarella et al., 2022; Zhang et al., 2020). Although existing studies have concerned the omission issue, an effective solution on a global scale is lacking (Huang et al., 2022; Liu et al., 2018). In this context, we proposed a multi-temporal CCDC algorithm that accounts for newly added ISA regions (NA-CCDC). This method improved the accuracy and completeness of ISA monitoring by enhancing representative ISA samples, with special focus on the ISA change regions (Fig. 23(a)-(d)).

On the other hand, in Fig. 23(e)-(h), ISA commissions originate from multiple land covers, including mining areas, rock, bare soil, and water bodies, due to their spectral similarity with ISA. At the global scale, the commissions of mining areas are found in Europe and North America (Fig. 23(f)), while rock and bare soil commissions are concentrated in the arid regions of the Middle East (Fig. 23(g)-(h)). Commissions caused by water bodies are common in China and India, and are often close to residential areas (Fig. 23(e)), increasing the difficulty for commission identification and removal. These ISA commissions show diverse characteristics, e.g., sizes and categories. In this context, we proposed the multi-scale iteration (MIA) algorithm to automatically remove global commissions, achieving satisfactory results (Fig. 23(e)-(h)).

## 6. Conclusions

In this study, we focused on the omission and commission issues in the existing 30 m global continuous ISA datasets. To address these issues, we proposed a series of novel algorithms and generated a new global ISA product, GISA-new. Specifically, for the omission problem, we proposed a multi-temporal CCDC algorithm that accounts for newly added ISA regions (NA-CCDC) to enhance the representativeness of samples in global ISA mapping. For the commission challenge, we introduced a multi-scale iterative algorithm to automatically remove global commissions, accounting for their diversity in sizes and types. The results showed that compared to GISA, WSF-evo, GAIA, and GAUD,

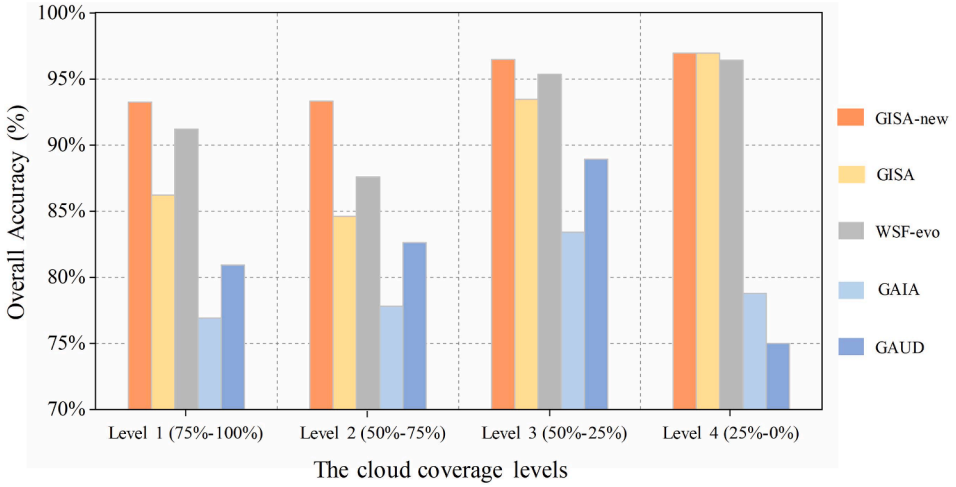


**Fig. 21.** Accuracy assessment under different cloud coverage conditions. The percentage of cloud cover is shown in parentheses.

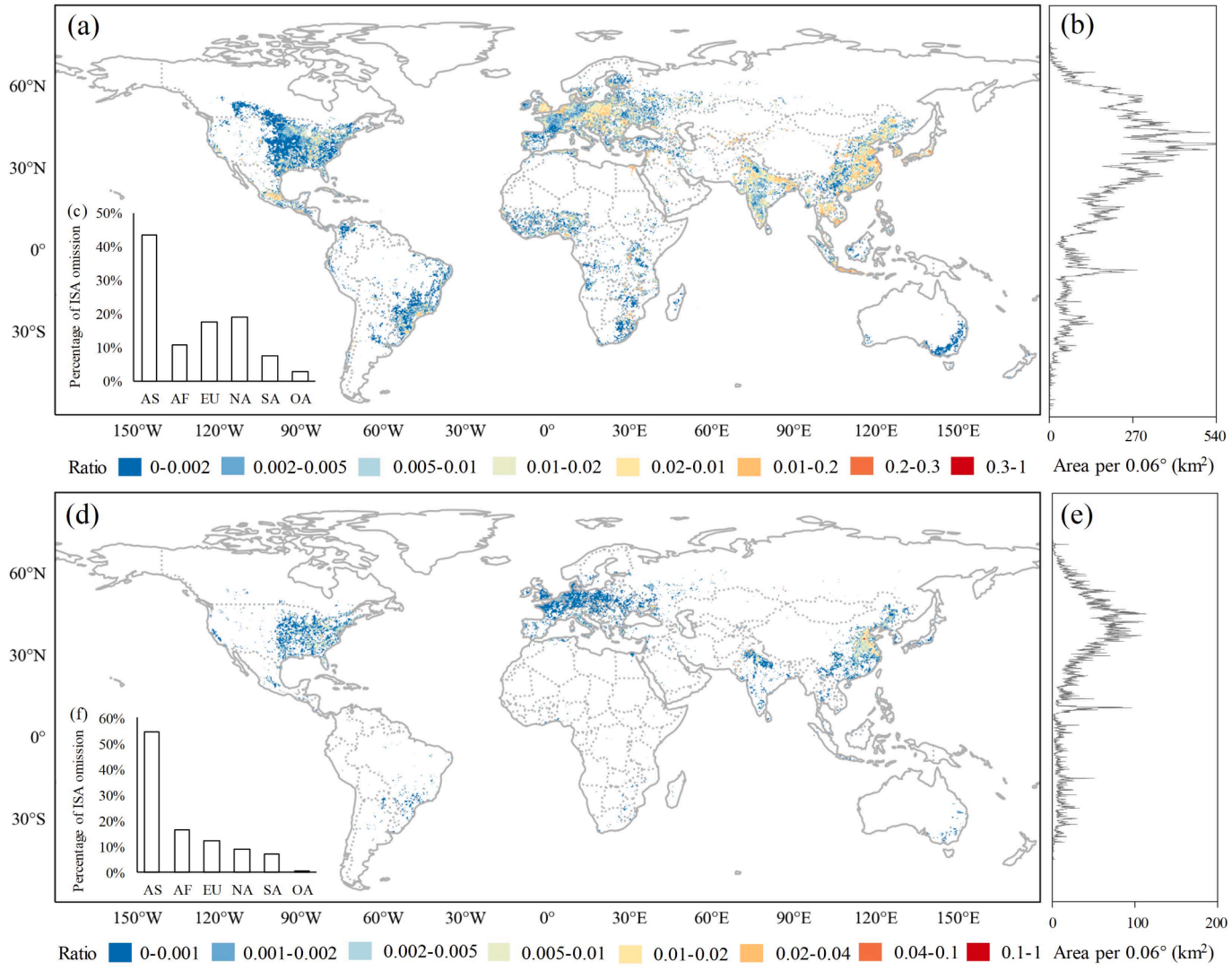


**Fig. 22.** The geographical distribution of global ISA omission and commission between 1985 and 2021. (a) and (d) represent the proportion of ISA omission and commission within 0.06∘ × 0.06∘ grids, respectively. (b) and (e) represent the latitudinal cumulative areas of ISA omission and commission, respectively. (c) and (f) represent the percentage of ISA omission and commission relative to the total ISA omission at the continental scale, respectively. AS: Asia, AF: Africa, EU: Europe, OA: Oceania, NA: North America, SA: South America.

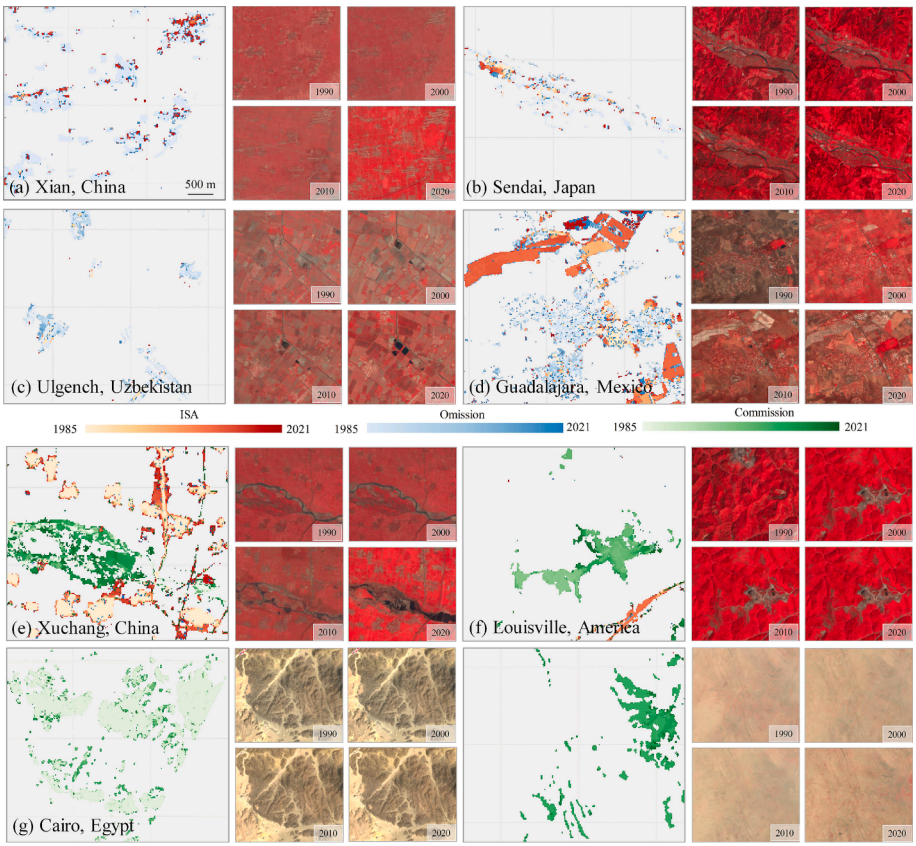


**Fig. 23.** Visualization of the results of ISA omission filling and commission removal in typical regions with various landscapes during 1985–2021. (a)-(d) represent omission examples; (e)-(f) represent commission examples.

GISA-new has the highest overall accuracy (OA) and F1-score, as well as the lowest omission and commission errors. Additionally, GISA-new demonstrated accuracy stability over the time series, further confirming its superiority. Based on GISA-new, the spatial distribution of global ISA omissions and commissions was investigated. It was found that ISA omissions and commissions have a wide distribution globally, but there was an imbalance between the southern and northern hemispheres. Generally speaking, the proposed method in this study effectively filled omissions in low-density impervious surfaces and removed global commissions caused by various land covers. The generated GISA-new has great potential to be used as fundamental data for global change and sustainable development assessments.

In the future, one possible research direction is deep learning mapping (Chen et al., 2023; Li et al., 2024). In recent years, deep learning techniques have made significant achievements in the urban remote sensing field, such as building extraction and building height estimation, which hold tremendous promise for further improving the accuracy of global ISA mapping. However, deep learning models usually rely on a large number of dense sample annotations, posing a challenge for large-scale ISA mapping. Another possible research direction is the aspect of application and analysis. To date, the existing global ISA datasets are not used worldwide for describing patterns and attribution of urbanization. In addition, most existing studies have focused on countries in the Global North, while neglecting countries in the Global South, especially in Africa. From the perspective of economic level, low-income and lower-middle-income countries have received less attention, even though these regions may experience faster urbanization in the future. From the perspective of population, small and medium-sized cities with populations of less than 1 million have been given less attention. According to the United Nations, small and medium-sized cities are expected to account for 54 % of the world's urban population by 2030 (United Nations, 2018). However, urbanization in these regions remains understudied. To this end, in the future, we will analyze the current status, trends, and impacts of urbanization in different regions, at different economic levels, and at different population densities, courtesy of more accurate global ISA datasets.

In addition, several limitations exist in the proposed method that need to be addressed in future. Firstly, uncertainties, such as omission and commission errors, remain in WSF 2019, ESA, and NTL, as none of these products are error-free. In the future, it is possible to use higher-resolution (e.g., sub-meter) data for global ISA mapping. For instance, Huang et al. (2024) generated China's first sub-meter (0.5 m) building footprint dataset (CBF) using deep learning.

Secondly, it should be noted that errors may arise from the commonly used assumption of ISA irreversibility, which deserves further investigation in future work.

## CRediT authorship contribution statement

**Huiqun Ren:** Writing – review & editing, Writing – original draft, Methodology, Conceptualization. **Xin Huang:** Writing – review & editing, Supervision, Resources, Conceptualization. **Jie Yang:** Writing – review & editing, Methodology, Conceptualization. **Guoqing Zhou:** Formal analysis, Writing – review & editing.

## Declaration of competing interest

The authors declare that they have no known competing financial interests or personal relationships that could have appeared to influence the work reported in this paper.

## Acknowledgments

The research was supported by the National Natural Science

Foundation of China (under Grant 42271328).

## References


Ban, Y., Jacob, A., Gamba, P., 2015. Spaceborne SAR data for global urban mapping at 30m resolution using a robust urban extractor. ISPRS J. Photogramm. Remote Sens. 103, 28–37. https://doi.org/10.1016/j.isprsjprs.2014.08.004.

Bovolo, F., Bruzzone, L., 2007. A theoretical framework for unsupervised change detection based on change vector analysis in the polar domain. IEEE Trans. Geosci. Remote Sens. 45, 218–236. https://doi.org/10.1109/TGRS.2006.885408.

Cai, B., Shao, Z., Huang, X., Zhou, X., Fang, S., 2023. Deep learning-based building height mapping using Sentinel-1 and Sentinel-2 data. Int. J. Appl. Earth Obs. Geoinf. 122. https://doi.org/10.1016/j.jag.2023.103399.

Chai, B., Li, P., 2023. An ensemble method for monitoring land cover changes in urban areas using dense Landsat time series data. ISPRS J. Photogramm. Remote Sens. 195, 29–42. https://doi.org/10.1016/j.isprsjprs.2022.11.002.

Chen, J., Chen, J., Liao, A., Cao, X., Chen, L., Chen, X., He, C., Han, G., Peng, S., Lu, M., Zhang, W., Tong, X., Mills, J., 2015. Global land cover mapping at 30m resolution: A POK-based operational approach. ISPRS J. Photogramm. Remote Sens. 103, 7–27. https://doi.org/10.1016/j.isprsjprs.2014.09.002.

Chen, T.-H.-K., Pandey, B., Seto, K.C., 2023. Detecting subpixel human settlements in mountains using deep learning: A case of the Hindu Kush Himalaya 1990–2020. Remote Sens. Environ. 294. https://doi.org/10.1016/j.rse.2023.113625.

Deng, C., Zhu, Z., 2020. Continuous subpixel monitoring of urban impervious surface using Landsat time series. Remote Sens. Environ. 238. https://doi.org/10.1016/j.rse.2018.10.011.

Elvidge, C.D., Zhizhin, M., Ghosh, T., Hsu, F.-C., Taneja, J., 2021. Annual time series of global VIIRS nighttime lights derived from monthly averages: 2012 to 2019. Remote Sens. 13. https://doi.org/10.3390/rs13050922.

Esch, T., Heldens, W., Hirner, A., Keil, M., Marconcini, M., Roth, A., Zeidler, J., Dech, S., Strano, E., 2017. Breaking new ground in mapping human settlements from space – The Global Urban Footprint. ISPRS J. Photogramm. Remote Sens. 134, 30–42. https://doi.org/10.1016/j.isprsjprs.2017.10.012.

Foody, G.M., Arora, M.K., 1997. An evaluation of some factors affecting the accuracy of classification by an artificial neural network. Int. J. Remote Sens. 18, 799–810. https://doi.org/10.1080/014311697218764.

Fu, P., Weng, Q., 2016. A time series analysis of urbanization induced land use and land cover change and its impact on land surface temperature with Landsat imagery. Remote Sens. Environ. 175, 205–214. https://doi.org/10.1016/j.rse.2015.12.040.

Gómez, C., White, J.C., Wulder, M.A., 2016. Optical remotely sensed time series data for land cover classification: A review. ISPRS J. Photogramm. Remote Sens. 116, 55–72. https://doi.org/10.1016/j.isprsjprs.2016.03.008.

Gong, P., Li, X., Zhang, W., 2019a. 40-Year (1978–2017) human settlement changes in China reflected by impervious surfaces from satellite remote sensing. Sci. Bull. 64, 756–763. https://doi.org/10.1016/j.scib.2019.04.024.

Gong, P., Liu, H., Zhang, M., Li, C., Wang, J., Huang, H., Clinton, N., Ji, L., Li, W., Bai, Y., Chen, B., Xu, B., Zhu, Z., Yuan, C., Ping Suen, H., Guo, J., Xu, N., Li, W., Zhao, Y., Yang, J., Yu, C., Wang, X., Fu, H., Yu, L., Dronova, I., Hui, F., Cheng, X., Shi, X., Xiao, F., Liu, Q., Song, L., 2019b. Stable classification with limited sample: transferring a 30-m resolution sample set collected in 2015 to mapping 10-m resolution global land cover in 2017. Sci. Bull. 64, 370–373. https://doi.org/10.1016/j.scib.2019.03.002.

Gong, P., Li, X., Wang, J., Bai, Y., Chen, B., Hu, T., Liu, X., Xu, B., Yang, J., Zhang, W., Zhou, Y., 2020. Annual maps of global artificial impervious area (GAIA) between 1985 and 2018. Remote Sens. Environ. 236. https://doi.org/10.1016/j.rse.2019.111510.

Gorelick, N., Hancher, M., Dixon, M., Ilyushchenko, S., Thau, D., Moore, R., 2017. Google Earth Engine: Planetary-scale geospatial analysis for everyone. Remote Sens. Environ. 202, 18–27. https://doi.org/10.1016/j.rse.2017.06.031.

Hafner, S., Ban, Y., Nascetti, A., 2022. Unsupervised domain adaptation for global urban extraction using Sentinel-1 SAR and Sentinel-2 MSI data. Remote Sens. Environ. 280. https://doi.org/10.1016/j.rse.2022.113192.

Herold, M., Latham, J.S., Di Gregorio, A., Schmullius, C.C., 2006. Evolving standards in land cover characterization. J. Land Use Sci. 1, 157–168. https://doi.org/10.1080/17474230601079316.

Huang, X., Li, J., Yang, J., Zhang, Z., Li, D., Liu, X., 2021. 30 m global impervious surface area dynamics and urban expansion pattern observed by Landsat satellites: From 1972 to 2019. Sci. China Earth Sci. 64, 1922–1933. https://doi.org/10.1007/s11430-020-9797-9.

Huang, H., Wang, J., Liu, C., Liang, L., Li, C., Gong, P., 2020. The migration of training samples towards dynamic global land cover mapping. ISPRS J. Photogramm. Remote Sens. 161, 27–36. https://doi.org/10.1016/j.isprsjprs.2020.01.010.

Huang, X., Yang, J., Wang, W., Liu, Z., 2022. Mapping 10 m global impervious surface area (GISA-10m) using multi-source geospatial data. Earth Syst. Sci. Data. 14, 3649–3672. https://doi.org/10.5194/essd-14-3649-2022.

Huang, X., Zhang, Z., Li, J., 2024. China's first sub-meter building footprints derived by deep learning. Remote Sens. Environ. 311, 114274. https://doi.org/10.1016/j.rse.2024.114274.

Li, X., Gong, P., Liang, L., 2015. A 30-year (1984–2013) record of annual urban dynamics of Beijing City derived from Landsat data. Remote Sens. Environ. 166, 78–90. https://doi.org/10.1016/j.rse.2015.06.007.

Li, C., Xian, G., Zhou, Q., Pengra, B.W., 2021. A novel automatic phenology learning (APL) method of training sample selection using multiple datasets for time-series land cover mapping. Remote Sens. Environ. 266. https://doi.org/10.1016/j.rse.2021.112670.

Li, C., Xian, G., Wellington, D., Smith, K., Horton, J., Zhou, Q., 2022. Development of the LCMAP annual land cover product across Hawai'i. Int. J. Appl. Earth Obs. Geoinf. 113, 103015. https://doi.org/10.1016/j.jag.2022.103015.

Li, Z., Zhang, A., Sun, G., Han, Z., Jia, X., 2024. Automatic impervious surface mapping in subtropical China via a terrain-guided gated fusion network. Int. J. Appl. Earth Obs. Geoinf. 127, 103608. https://doi.org/10.1016/j.jag.2023.103608.

Li, X., Zhou, Y., Zhu, Z., Liang, L., Yu, B., Cao, W., 2018. Mapping annual urban dynamics (1985–2015) using time series of Landsat data. Remote Sens. Environ. 216, 674–683. https://doi.org/10.1016/j.rse.2018.07.030.

Li, X., Zhou, Y., Eom, J., Yu, S., Asrar, G.R., 2019. Projecting global urban area growth through 2100 based on historical time series data and future shared socioeconomic pathways. Earth's Future. 7, 351–362. https://doi.org/10.1029/2019ef001152.

Li, X., Gong, P., Zhou, Y., Wang, J., Bai, Y., Chen, B., Hu, T., Xiao, Y., Xu, B., Yang, J., Liu, X., Cai, W., Huang, H., Wu, T., Wang, X., Lin, P., Li, X., Chen, J., He, C., Li, X., Yu, L., Clinton, N., Zhu, Z., 2020. Mapping global urban boundaries from the global artificial impervious area (GAIA) data. Environ. Res. Lett. 15, 094044. https://doi.org/10.1088/1748-9326/ab9be3.

Liu, X., Hu, G., Chen, Y., Li, X., Xu, X., Li, S., Pei, F., Wang, S., 2018. High-resolution multi-temporal mapping of global urban land using Landsat images based on the Google Earth Engine Platform. Remote Sens. Environ. 209, 227–239. https://doi.org/10.1016/j.rse.2018.02.055.

Liu, C., Huang, X., Zhu, Z., Chen, H., Tang, X., Gong, J., 2019. Automatic extraction of built-up area from ZY3 multi-view satellite imagery: Analysis of 45 global cities. Remote Sens. Environ. 226, 51–73. https://doi.org/10.1016/j.rse.2019.03.033.

Liu, X., Huang, Y., Xu, X., Li, X., Li, X., Ciais, P., Lin, P., Gong, K., Ziegler, A.D., Chen, A., Gong, P., Chen, J., Hu, G., Chen, Y., Wang, S., Wu, Q., Huang, K., Estes, L., Zeng, Z., 2020. High-spatiotemporal-resolution mapping of global urban change from 1985 to 2015. Nat. Sustain. 3, 564–570. https://doi.org/10.1038/s41893-020-0521-x.

Loveland, T.R., Belward, A.S., 1997. The International Geosphere Biosphere Programme Data and Information System global land cover data set (DISCover). Acta Astronautica. 41, 681–689. https://doi.org/10.1016/S0094-5765(98)00050-2.

Ma, T., Zhou, C., Pei, T., Haynie, S., Fan, J., 2014. Responses of Suomi-NPP VIIRS-derived nighttime lights to socioeconomic activity in China's cities. Remote Sens. Lett. 5, 165–174. https://doi.org/10.1080/2150704x.2014.890758.

Marconcini, M., Metz- Marconcini, A., Esch, T., Gorelick, N., 2021. Understanding Current Trends in Global Urbanisation - The World Settlement Footprint Suite. GI_Forum. 1, 33-38. Doi: 10.1553/giscience2021_01_s33.

Masek, J.G., Vermote, E.F., Saleous, N.E., Wolfe, R., Hall, F.G., Huemmrich, K.F., Gao, F., Kutler, J., Lim, T.K., 2006. A Landsat Surface Reflectance Dataset for North America, 1990–2000. IEEE Geosci. Remote Sens. Lett. 3, 68–72. https://doi.org/10.1109/lgrs.2005.857030.

Microsoft, 2022. Microsoft Releases 770 Million Building Footprints in the US as Open Data. https://github.com/microsoft/GlobalMLBuildingFootprints, Accessed: 18 July 2022.

Olson, D.M., Dinerstein, E., Wikramanayake, E.D., Burgess, N.D., Powell, G.V.N., Underwood, E.C., D'amico, J.A., Itoua, I., Strand, H.E., Morrison, J.C., Loucks, C.J., Allnutt, T.F., Ricketts, T.H., Kura, Y., Lamoreux, J.F., Wettengel, W.W., Hedao, P., Kassem, K.R., 2001. Terrestrial Ecoregions of the World: A New Map of Life on Earth: A new global map of terrestrial ecoregions provides an innovative tool for conserving biodiversity. Bioscience. 51, 933–938. https://doi.org/10.1641/0006-3568(2001)051[0933:Teotwa]2.0.Co;2.

Pasquarella, V.J., Arévalo, P., Bratley, K.H., Bullock, E.L., Gorelick, N., Yang, Z., Kennedy, R.E., 2022. Demystifying LandTrendr and CCDC temporal segmentation. Int. J. Appl. Earth Obs. Geoinf. 110. https://doi.org/10.1016/j.jag.2022.102806.

Seto, K.C., Fragkias, M., Guneralp, B., Reilly, M.K., 2011. A meta-analysis of global urban land expansion. PLoS ONE. 6, e23777. https://doi.org/10.1371/journal.pone.0023777.

Seto, K.C., Guneralp, B., Hutyra, L.R., 2012. Global forecasts of urban expansion to 2030 and direct impacts on biodiversity and carbon pools. Proc. Natl. Acad. Sci. u. s. a. 109, 16083–16088. https://doi.org/10.1073/pnas.1211658109.

Shi, K., Yu, B., Huang, Y., Hu, Y., Yin, B., Chen, Z., Chen, L., Wu, J., 2014. Evaluating the ability of NPP-VIIRS Nighttime Light data to estimate the gross domestic product and the electric power consumption of china at multiple scales: a comparison with DMSP-OLS Data. Remote Sens. 6, 1705–1724. https://doi.org/10.3390/rs6021705.

Stehman, S.V., Foody, G.M., 2019. Key issues in rigorous accuracy assessment of land cover products. Remote Sens. Environ. 231. https://doi.org/10.1016/j.rse.2019.05.018.

Sulla-Menashe, D., Gray, J.M., Abercrombie, S.P., Friedl, M.A., 2019. Hierarchical mapping of annual global land cover 2001 to present: The MODIS Collection 6 Land Cover product. Remote Sens. Environ. 222, 183–194. https://doi.org/10.1016/j.rse.2018.12.013.

Tian, Y., Chen, H., Song, Q., Zheng, K., 2018. A novel index for impervious surface area mapping: development and validation. Remote Sens. 10, 1521.

United Nations, 2018. 2018 Revision of World Urbanization Prospect. , Accessed: 22 December 2023.

United Nations, 2022. World Cities Report 2022. , Accessed: 22 December 2023.

Verbesselt, J., Hyndman, R., Newnham, G., Culvenor, D., 2010. Detecting trend and seasonal changes in satellite image time series. Remote Sens. Environ. 114, 106–115. https://doi.org/10.1016/j.rse.2009.08.014.

Vermote, E., Justice, C., Claverie, M., Franch, B., 2016. Preliminary analysis of the performance of the Landsat 8/OLI land surface reflectance product. Remote Sens. Environ. 185, 46–56. https://doi.org/10.1016/j.rse.2016.04.008.

Wang, L., Li, C., Ying, Q., Cheng, X., Wang, X., Li, X., Hu, L., Liang, L., Yu, L., Huang, H., Gong, P., 2012. China's urban expansion from 1990 to 2010 determined with satellite remote sensing. Chin. Sci. Bull. 57, 2802–2812. https://doi.org/10.1007/s11434-012-5235-7.

Wang, Y., Li, M., 2019. Urban impervious surface detection from remote sensing images: a review of the methods and challenges. IEEE Geosci. Remote Sens. Mag. 7, 64–93. https://doi.org/10.1109/mgrs.2019.2927260.

Wang, M., Mao, D., Wang, Y., Li, H., Zhen, J., Xiang, H., Ren, Y., Jia, M., Song, K., Wang, Z., 2024. Interannual changes of urban wetlands in China's major cities from 1985 to 2022. ISPRS J. Photogramm. Remote Sens. 209, 383–397. https://doi.org/10.1016/j.isprsjprs.2024.02.011.

Wang, Y., Sun, Y., Cao, X., Wang, Y., Zhang, W., Cheng, X., 2023. A review of regional and Global scale Land Use/Land Cover (LULC) mapping products generated from satellite remote sensing. ISPRS J. Photogramm. Remote Sens. 206, 311–334. https://doi.org/10.1016/j.isprsjprs.2023.11.014.

Weng, Q., 2012. Remote sensing of impervious surfaces in the urban areas: Requirements, methods, and trends. Remote Sens. Environ. 117, 34–49. https://doi.org/10.1016/j.rse.2011.02.030.

Wu, Y., Shi, K., Chen, Z., Liu, S., Chang, Z., 2022. Developing Improved Time-Series DMSP-OLS-Like Data (1992–2019) in China by Integrating DMSP-OLS and SNPP-VIIRS. IEEE Trans. Geosci. Remote Sens. 60, 1–14. https://doi.org/10.1109/tgrs.2021.3135333.

Xie, S., Liu, L., Zhang, X., Yang, J., 2022. Mapping the annual dynamics of land cover in Beijing from 2001 to 2020 using Landsat dense time series stack. ISPRS J. Photogramm. Remote Sens. 185, 201–218. https://doi.org/10.1016/j.isprsjprs.2022.01.014.

Yang, J., Huang, X., 2021. The 30 m annual land cover dataset and its dynamics in China from 1990 to 2019. Earth Syst. Sci. Data. 13, 3907–3925. https://doi.org/10.5194/essd-13-3907-2021.

Zanaga, D., Van De Kerchove, R., Daems, D., De Keersmaecker, W., Brockmann, C., Kirches, G., Wevers, J., Cartus, O., Santoro, M., Fritz, S., Lesiv, M., Herold, M., Tsendbazar, N. E., Xu, P., Ramoino, F., Arino, O., 2020. ESA WorldCover 10 m 2020 v100.

Zanaga, D., Van De Kerchove, R., Daems, D., De Keersmaecker, W., Brockmann, C., Kirches, G., Wevers, J., Cartus, O., Santoro, M., Fritz, S., Lesiv, M., Herold, M., Tsendbazar, N. E., Xu, P., Ramoino, F., Arino, O., 2022. ESA WorldCover 10 m 2021 v200.

Zhang, C., Dong, J., Xie, Y., Zhang, X., Ge, Q., 2022a. Mapping irrigated croplands in China using a synergetic training sample generating method, machine learning classifier, and Google Earth Engine. Int. J. Appl. Earth Obs. Geoinf. 112. https://doi.org/10.1016/j.jag.2022.102888.

Zhang, X., Liu, L., Wu, C., Chen, X., Gao, Y., Xie, S., Zhang, B., 2020. Development of a global 30 m impervious surface map using multisource and multitemporal remote sensing datasets with the Google Earth Engine platform. Earth Syst. Sci. Data. 12, 1625–1648. https://doi.org/10.5194/essd-12-1625-2020.

Zhang, X., Liu, L., Zhao, T., Gao, Y., Chen, X., Mi, J., 2022b. GISD30: global 30 m impervious-surface dynamic dataset from 1985 to 2020 using time-series Landsat imagery on the Google Earth Engine platform. Earth Syst. Sci. Data. 14, 1831–1856. https://doi.org/10.5194/essd-14-1831-2022.

Zhang, Z., Qian, Z., Zhong, T., Chen, M., Zhang, K., Yang, Y., Zhu, R., Zhang, F., Zhang, H., Zhou, F., Yu, J., Zhang, B., Lu, G., Yan, J., 2022c. Vectorized rooftop area data for 90 cities in China. Sci. Data. 9, 66. https://doi.org/10.1038/s41597-022-01168-x.

Zhang, Q., Zhang, Z., Xu, N., Li, Y., 2023. Fully automatic training sample collection for detecting multi-decadal inland/seaward urban sprawl. Remote Sens. Environ. 298. https://doi.org/10.1016/j.rse.2023.113801.

Zhao, M., Zhou, Y., Li, X., Zhou, C., Cheng, W., Li, M., Huang, K., 2020. Building a Series of Consistent Night-Time Light Data (1992–2018) in Southeast Asia by Integrating DMSP-OLS and NPP-VIIRS. IEEE Trans. Geosci. Remote Sens. 58, 1843–1856. https://doi.org/10.1109/tgrs.2019.2949797.

Zheng, Y., Tang, L., Wang, H., 2021. An improved approach for monitoring urban built-up areas by combining NPP-VIIRS nighttime light, NDVI, NDWI, and NDBI. J. Clean. Prod. 328, 129488. https://doi.org/10.1016/j.jclepro.2021.129488.

Zhou, Y., Li, X., Asrar, G.R., Smith, S.J., Imhoff, M., 2018. A global record of annual urban dynamics (1992–2013) from nighttime lights. Remote Sens. Environ. 219, 206–220. https://doi.org/10.1016/j.rse.2018.10.015.

Zhou, Y., Li, C., Zheng, W., Rong, Y., Liu, W., 2021. Identification of urban shrinkage using NPP-VIIRS nighttime light data at the county level in China. Cities. 118. https://doi.org/10.1016/j.cities.2021.103373.

Zhu, Z., 2017. Change detection using landsat time series: a review of frequencies, preprocessing, algorithms, and applications. ISPRS J. Photogramm. Remote Sens. 130, 370–384. https://doi.org/10.1016/j.isprsjprs.2017.06.013.

Zhu, Z., Woodcock, C.E., 2014a. Automated cloud, cloud shadow, and snow detection in multitemporal Landsat data: An algorithm designed specifically for monitoring land cover change. Remote Sens. Environ. 152, 217–234. https://doi.org/10.1016/j.rse.2014.06.012.

Zhu, Z., Gallant, A.L., Woodcock, C.E., Pengra, B., Olofsson, P., Loveland, T.R., Jin, S., Dahal, D., Yang, L., Auch, R.F., 2016. Optimizing selection of training and auxiliary data for operational land cover classification for the LCMAP initiative. ISPRS J. Photogramm. Remote Sens. 122, 206–221. https://doi.org/10.1016/j.isprsjprs.2016.11.004.

Zhu, Z., Woodcock, C.E., 2014b. Continuous change detection and classification of land cover using all available Landsat data. Remote Sens. Environ. 144, 152–171. https://doi.org/10.1016/j.rse.2014.01.011.